

Doctoral Dissertation

**Investigating the indeterminacy and inaccuracy of camera
intrinsic parameters in Unmanned-Aerial-Vehicle-based
photogrammetry using structure from motion**

(SfM を使った UAV 写真測量における内部パラメータの推定の不定性と不正確性に関する研究)

September, 2025

HO THANH TRUC

Graduate School of Sciences and Technology for Innovation,
Yamaguchi University

Acknowledgement

This dissertation is a tribute to all the individuals who have made my academic journey meaningful.

First and foremost, I would like to express my deepest gratitude to the Ministry of Education, Culture, Sports, Science and Technology (MEXT), Japan, for awarding me the Monbukagakusho Scholarship from September 2021 to September 2025. Without this financial support, this study would not have been possible.

I am profoundly indebted to my supervisor, Associate Professor Ariyo Kanno, for his continuous guidance, patience, and immense knowledge. His invaluable support has shaped every stage of my doctoral research and the writing of this dissertation. I could not have asked for a better advisor and mentor.

My sincere thanks also go to the professors of “Eisei Laboratory”: Prof. Masahiko Sekine, Prof. Tsuyoshi Imai, Prof. Takaya Higuchi, and Prof. Koichi Yamamoto. Their insightful comments and critical questions during our regular English seminars significantly enriched my research from multiple perspectives.

I am also grateful to the members of my doctoral dissertation defense committee - Prof. Yoshiki Mizukami, Prof. Takaya Higuchi, Prof. Koichi Yamamoto, Assoc. Prof. Shinichiro Nakashima, and Assoc. Prof. Ariyo Kanno (chair) - for their constructive criticisms and valuable suggestions, which have helped refine this work.

Equally important are the friendships that made my doctoral journey joyful and fulfilling. I deeply appreciate Takata, Kakiyara, Kon, Sato, Nina, Kagawa, and all past and present members of the Kanno Laboratory for their stimulating discussions, encouragement, and the memorable times we shared.

Most importantly, I owe heartfelt gratitude to my family. To my parents, my younger sister, and brother, thank you for your unconditional love and constant encouragement. A special note of appreciation goes to my beloved husband, Vo Thanh Huy, my daughter, Vo Ho To Quyen, and my son, Vo Thanh Hoang, whose patience, understanding, and unwavering belief in me have been the cornerstone of my resilience and success.

Finally, I would like to acknowledge myself. This doctoral journey has been one of challenges, perseverance, and profound personal growth. I am proud of the determination and effort I invested in pursuing my academic goals. This process has strengthened my belief in resilience, self-confidence, and the pursuit of excellence. I am grateful for the opportunity to learn, to grow, and to contribute to my field of study.

Summaries

Aerial photogrammetry using Unmanned Aerial Vehicles (UAV) has emerged as a powerful technique for generating high-resolution three-dimensional (3D) models across various domains, including infrastructure inspection, mining surveying, hazard modeling, and environmental monitoring. Structure from motion (SfM) forms the foundation of this technique, enabling simultaneous estimation of camera intrinsic and extrinsic parameters and facilitating the creation of 3D products such as dense point clouds via Multi-View Stereo (MVS). Enhancing the reliability of UAV-based photogrammetry using SfM, while minimizing ground measurements such as ground control points (GCPs), is highly desirable.

Recently, relatively expensive RTK drones equipped with RTK-GNSS receivers - capable of recording the latitude, longitude, and altitude of the optical center of each image with centimeter-level accuracy - have gained popularity. This advancement provides auxiliary information for SfM to improve the accuracy of camera parameter estimation and, in turn, enhance the accuracy of UAV-based photogrammetry. However, several practical issues in the SfM process can potentially degrade the final model accuracy. Specially, these include:

1. Concerns about accuracy degradation due to non-optimal SfM analysis settings

SfM involves many analysis setting parameters, but most previous studies have evaluated the accuracy and precision of SfM using only standard analysis settings. Thus, the influence of analysis settings on SfM accuracy and precision remains unclear. Since the optimal settings differ by image set and are typically unknown in practical situations, it is important to identify image acquisition methods that are robust to non-optimal analysis settings. Recent reports suggest that CPA-2D-GP (Constant-Pitch-Angle, Two-Directional, and Gridded-Position) flight design with pitch angles of 20° – 35° may be robust under such conditions, but further validation under broader conditions is necessary.

2. Indeterminacy of intrinsic parameters in image-based SfM using non-RTK drone data

In UAV-based photogrammetry, SfM with self-calibration is commonly used to estimate camera intrinsic parameters. However, when SfM is performed using only images - referred to as image-based SfM, and the combination of shooting method and scene geometry falls into a critical configuration, certain intrinsic parameters may become indeterminate, resulting in inaccurate outcomes. It remains unclear which intrinsic parameters may be indeterminate, under which combinations of camera motion and scene geometry and how it manifests in practice.

3. Introduction of inaccuracies in intrinsic parameter estimation due to in-camera distortion correction

SfM typically applies lens distortion correction using the Brown model, under the assumption that no prior distortion correction has been applied to the input images. However, some UAV cameras

perform manufacturer-specific geometric corrections when saving images. Applying the Brown model to such pre-corrected images may introduce additional errors in intrinsic parameter estimation.

To address these issues, this study conducted three investigations:

First, the robustness of SfM accuracy and precision across different analysis settings was examined using 15 image-sets and 750 analysis settings. Images captured at three different GSDs and five pitch angles by the CPA-2D-GP flight design were exploited in this study. SfM was performed for 750 analysis settings with camera coordinates measured by RTK-GNSS integrated into the bundle adjustment (BA). Results demonstrated that CPA-2D-GP flight design with 20° and 30° pitch angles was the most robust against the non-optimality in SfM settings, with RMS errors for all validation points not exceeding 0.056 m. These results suggest that employing these pitch angles minimizes concerns related to SfM settings, and yields the most stable estimation of intrinsic parameters. These findings confirmed the generality of the robustness of CPA-2D-GP flight design against non-optimal SfM settings, as suggested by the previous research.

Second, the indeterminacy of intrinsic parameters in SfM was examined using images captured by Constant-Pitch-Angle, One-Directional, and Gridded-Position (CPA-1D-GP) flight design. Numerical experiments demonstrated that the focal length (f) and principal point coordinate (c_y) were indeterminable in images acquired under ideal conditions, where the UAV maintained a perfectly constant altitude and orientation across strips. This indeterminacy was also confirmed in real datasets, manifested as instability of intrinsic parameter estimation across 30 different SfM settings and in 50 repeated trials under a standard setting. However, introducing intermediate strips to transform CPA-1D-GP into CPA-2D-GP flight design effectively mitigated this issue.

Finally, this study evaluated inaccuracies introduced by in-camera distortion correction applied during image saving, prior to the SfM process, by focusing on its effect on systematic deformation in digital elevation models (DEMs) derived from images captured using CPA-2D-GP flight design. DEMs generated from images with and without distortion correction were compared to reference DEMs. The results showed that, in image-based SfM, DEM deformation occurred regardless of whether in-camera distortion correction was applied. However, when camera coordinates were integrated into the bundle adjustment for optimizing camera parameters, the deformation was eliminated.

In conclusion, this study systematically investigated practical issues related to the indeterminacy and inaccuracy of intrinsic parameters in UAV-based photogrammetry using SfM, and proposed experimentally validated strategies to mitigate these issues.

Table of Contents

CHAPTER 1. INTRODUCTION	1
1.1. Background	1
1.2. Objectives	3
1.3. Thesis structure	4
1.4. Publications	5
CHAPTER 2. FUNDAMENTALS OF UAV-BASED PHOTOGRAMMETRY AND STRUCTURE FROM MOTION	7
2.1. UAV-based photogrammetry	7
2.2. Intrinsic parameters estimation	8
2.2.1. Radial and tangential distortions.	8
2.2.2. Brown-Conrady distortion model.....	9
2.3. Structure from Motion	10
2.4. UAV flight design	13
2.5. Analysis settings in SfM	14
2.5.1. Align photos	14
2.5.2. Reference settings	15
2.5.3. Optimize camera alignment.....	15
CHAPTER 3. ROBUSTNESS OF SFM ACCURACY AND PRECISION AGAINST NON- OPTIMALITY IN ANALYSIS SETTINGS.....	17
3.1. Introduction	17
3.2. Methods	17
3.2.1. Data acquisition	17
3.2.2. SfM processing	19
3.2.3. Error evaluation and comparison	20
3.2.4. Alignment failure and valid matching tallying	21
3.3. Results	22
3.3.1. SfM accuracy and precision for image-sets taken at 0° pitch angle.....	22
3.3.2. Robustness of SfM accuracy and precision against non-optimal SfM analysis settings.	22
3.3.3. Correlation between the mean vertical error of all validation points and the estimated intrinsic parameters.	24
3.3.4. Alignment failure and valid matching	25
3.4. Discussion	26
3.4.1. Pitch angles robust against non-optimal analysis settings	26
3.4.2. Pitch angles not robust against non-optimal analysis settings	27
3.4.3. Limitations and future research	28
3.5. Conclusion	28
CHAPTER 4. INDETERMINACY OF CAMERA INTRINSIC PARAMETERS IN STRUCTURE FROM MOTION USING IMAGES FROM CONSTANT-PITCH ANGLE FLIGHT DESIGN ..	30
4.1. Introduction	30
4.2. Methods	30
4.2.1. Fundamental of self-calibration in SfM	30
4.2.2. Numerical experiments	31
4.2.3. Real-data analysis	36

4.3. Results	39
4.3.1. Numerical experiments	39
4.3.2. Real-data analysis	41
4.4. Discussion	44
4.4.1. Indeterminacy of camera intrinsic parameters in images-based SfM	44
4.4.2. Remedy for indeterminacy of intrinsic parameters in images-based SfM.....	44
4.4.3. Implications for common flight configurations	45
4.5. Conclusion	45
CHAPTER 5. IMPACT OF IN-CAMERA DISTORTION CORRECTION ON SYSTEMATIC DEFORMATION IN UAV-BASED PHOTOGRAMMETRY USING STRUCTURE FROM MOTION	47
5.1. Introduction	47
5.2. Methods	48
5.2.1. Data acquisition	48
5.2.2. Simulation of in-camera distortion correction	48
5.2.3. SfM processing and systematic deformation evaluation	49
5.3. Results and discussion	51
5.3.1. Differences between the reference DEMs and DEMs with in-camera distortion correction	51
5.3.2. Evaluation of the magnitude of deformation	52
5.4. Conclusion	55
CHAPTER 6. CONCLUSION AND FUTURE RESEARCH	56
6.1. Conclusion	56
6.2. Future research.....	57

List of Abbreviation

BA	Bundle adjustment
CPA	Constant-Pitch-Angle
CPA-1D-GP	Constant-Pitch-Angle, One-Directional and Gridded-Position
CPA-2D-GP	Constant-Pitch-Angle, Two-Directional, and Gridded-Position
CPA-1D-RP	Constant-Pitch-Angle, One-Directional and Random-Position
DEM	Digital Elevation Model
GCP	Ground Control Point
GNSS	Global Navigation Satellite System
GSD	Ground Sample Distance
MVS	Multi-view Stereo
RMS Error	Root Mean Square Error
RTK-GNSS	Real-Time Kinematic Global Navigation Satellite System
SfM	Structure-from-Motion
UAV	Unmanned Aerial Vehicle
Val_RMSE_T	Total RMS error of all validation points
Val_RMSE_Z	Vertical RMS error of all validation points

List of Figures

Figure 2-1. Coordinate transformation from 3D point to 2D.	7
Figure 2-2. Pinhole projection of a 3D point X onto a camera image plane.	8
Figure 2-3. Effect of radial distortion on a square grid.	9
Figure 2-4. Effect of tangential distortion. The solid lines represent case of no distortion and dashed lines are with tangential distortion (right) and (left) how tangential and radial distortion shifts a pixel from its ideal position.	9
Figure 2-5. UAV SfM-photogrammetry workflow for generating a dense point cloud.	11
Figure 2-6. Reprojection error calculation	12
Figure 2-7. CPA-2D-GP and CPA-1D-GP flight design at 20° pitch angle.	14
Figure 3-1. Actual terrain situation captured by pitch angle of 40° of GSD15 for bare land (a) and vegetation covering area (b).	18
Figure 3-2. Distribution of camera positions and validation points at the study site overlaid with orthophotos generated by GSD 10 (a), GSD 15 (b), and GSD 20 (c).	18
Figure 3-3. Main strip (named as ST) in images.	21
Figure 3-4. Correlation between the mean vertical error of all validation points (MEZ) and estimated f in image-sets of 10° pitch angle (a) GSD 10; (b) GSD 15; (c) GSD 20.	25
Figure 4-1. Example of a critical configuration where the focal length f cannot be determined from parallel shooting images.	32
Figure 4-2. Two views of the target used for image acquisition in the numerical experiments: (a) Side view; (b) Front view.	32
Figure 4-3. SfM flow in numerical experiments to evaluate the indeterminacy of each intrinsic parameter (f or cy).	35
Figure 4-4. Camera positions and validation points at the study site overlaid with orthophotos generated by GSD10 (a), GSD15 (b), GSD20 (c) using CPA-2D-GP flight design. At each validation point, world coordinates were measured by Aerobo markers (d) with a built-in GNSS receiver.	36
Figure 4-5. Generation of CPA-1D-GP flight design from CPA-2D-GP flight design used in real-data analysis	37
Figure 4-6. RMS reprojection error and estimated parameter values when fixing parameter f or cy to incorrect values for six flight designs.	40
Figure 4-7. Rate of increase in rms reprojection error when fixing parameter f or cy to incorrect values for six flight designs.	40
Figure 4-8. Intrinsic parameter estimation and statistics of total RMS error (Val_RMSE_T) and vertical RMS error (Val_RMSE_Z) of all validation points for each image-set (one SfM analysis setting with 50 trials).	41
Figure 4-9. Intrinsic parameter estimation and statistics of total RMS error (Val_RMSE_T) and vertical RMS Error (Val_RMSE_Z) of all validation points for each image-set (30 analysis settings).	42
Figure 4-10. The correlation between estimated f and mean vertical error (MEZ).	43
Figure 5-1. Systematic deformation in the form of doming or bowling [15].	47
Figure 5-2. Constant-Pitch-Angle, Two-Directional, and Gridded-Position flight design (CPA-2D-GP) at 20° pitch angle (from Metashape).	48
Figure 5-3. SfM workflow and research procedure	50
Figure 5-4. Identifying systematic deformation through visualization of the differential DEM	50

List of Tables

Table 3-1. Meteorological conditions during image acquisition.....	17
Table 3-2. Summary of the 15 flights used in this study.....	19
Table 3-3. Summary of the analysis settings tested in this study.....	20
Table 3-4. Statistics of RMS error of all validation points for 0° pitch angle image-sets.....	23
Table 3-5. Statistics of RMS error of all validation points and intrinsic parameters for each image-set (750 analysis settings with 2 trials of each setting)	23
Table 3-6. Average ratio of adjacent inter-strip matchings to intra-strip matchings for main-strips under a standard SfM setting observed in 20° and 40° pitch angles in three GSDs.....	26
Table 3-7. Percentage of adjacent inter-strip matching to intra-strip matching in main-strips in single SfM setting for image-sets with 40° pitch angle.	26
Table 4-1. Camera specifications used in CG space	32
Table 4-2. Classification of flight designs in numerical experiments	33
Table 4-3. Descriptions of six image-sets taken by six flight designs in numerical experiments....	33
Table 4-4. Settings for “Alignment” used to generate accurate tie points.	35
Table 4-5. Summary of three CPA-2D-GP flights acquired by P4RTK and three CPA-1D-GP flights in real-data analysis.....	37
Table 4-6. Summary of the analysis settings tested in this study.....	38
Table 4-7. Average of vertical error ratio for each image-set (30 SfM analysis settings)	43
Table 5-1. Details of raw image sets acquired without in-camera distortion correction. Images were exported in their original (uncorrected) format.	48
Table 5-2. Differential DEMs calculated from Workflow 1: Bundle adjustment using RTK-GNSS camera positions.....	51
Table 5-3. Differential DEMs calculated from Workflow 2: Bundle adjustment using images only.	52
Table 5-4. Spatial distribution of 95 th percentile pixel values (Red) and 5 th percentile pixel values (blue) in DEM _{difference} for Workflow 2.	53
Table 5-5. Histograms of pixel values of DEM _{difference} with 95 th percentile (Red) and 5 th percentile (blue) for Workflow 2.	53
Table 5-6. Spatial distribution of 95 th percentile pixel values (Red) and 5 th percentile pixel values (blue) in DEM _{difference} for Workflow 2, after applying maximum local slope filtering.....	55

Chapter 1. Introduction

1.1. Background

Unmanned aerial vehicle (UAV)-based photogrammetry is a technique of reconstructing the three-dimensional (3D) models of target area from overlapping images acquired from UAVs. In recent years, it has emerged a dominant method for acquiring high-resolution spatial data efficiently and cost-effectively. This technique has been widely adopted in various domains such as infrastructure inspection, mining surveys, hazard modeling, and environmental monitoring. For example, this method is utilized to obtain digital elevation models (DEMs), digital surface models (DSMs) for environmental monitoring [1–3] or mining surveying and landslide modeling [4–6], as well as to acquire shallow-water bathymetric data [7,8]. The rapid adoption of UAV-based photogrammetry is largely driven by advances in technology, including the proliferation of low-cost UAVs, user-friendly flight planning software, and Structure from Motion with Multi-View Stereo (SfM-MVS) processing tools.

The backbone of UAV-based photogrammetry is Structure from motion (SfM), which reconstructs 3D geometry from overlapping 2D images by estimating camera parameters (intrinsic and extrinsic parameters). These parameters are further refined through bundle adjustment (BA) and subsequently used in MVS to generate a dense point cloud. Therefore, the accuracy of the SfM process is a key factor influencing the MVS process and the final derived models, such as 3D meshes or DEMs.

Several factors can affect the accuracy and precision of UAV-based photogrammetry using SfM. The impact of flight height, the number and distribution of ground control points (GCPs) has been extensively investigated [4,9–11]. Sanz-Ablanedo et al. (2018) [12] demonstrated that evenly distributing GCPs across a target area of several km² - ideally in a triangular mesh grid - yields RMS errors approximately twice the average GSD when using more than two GCPs per 100 images. According to Aydin and Yakar (2023) [13], drones flown at lower altitudes achieved higher vertical accuracy, as a 70-meter increase in flight height resulted in a 3 cm decrease in vertical accuracy, while horizontal accuracy remained largely unaffected. Recently, drones equipped with onboard RTK-GNSS receivers have emerged, providing centimeter-level camera position of each image's optical center. This allows SfM to incorporate these precise camera positions into BA to improve the estimation of camera parameters and georeferencing, which in turn, enhances the accuracy of UAV-based photogrammetry [14,15]. Despite their benefits, GCPs and RTK-GNSS are costly and time-consuming to collect, especially in large or hazardous areas. Therefore, it is desired to improve the reliability of UAV photogrammetry using SfM while minimizing reliance on external field

measurements.

In addition to field data, flight design (i.e., image acquisition plan) and analysis settings in SfM process significantly influence the SfM performance. For instance, a better flight design can improve camera parameters estimation, thereby enhance the accuracy and precision of SfM [9,16,17]. Various UAV flight designs have been investigated. Among these, the constant-pitch-angle (CPA) flight design is widely adopted [18–23]. In this flight design, the camera is tilted at a fixed pitch angle along each flight strip. When UAVs fly in opposing directions, local convergence of viewing angles is achieved, facilitating more effective 3D reconstruction.

However, several practical issues in the SfM process can degrade the final model accuracy.

The analysis settings used in the SfM software can greatly influence the accuracy and precision of SfM. Adjusting settings related to feature points detection and bundle adjustment procedures in SfM can significantly change its results. Despite this, most existing studies have predominantly focused on evaluating SfM performance using a single analysis setting (e.g., the default settings) [16], [17], [18], [21]. Takata et al. (2021) [24] observed that SfM performance can be robust against non-optimal settings when using Constant-Pitch-Angle, Two-Directional, and Gridded-Position (CPA-2D-GP) flight design with 20°-35° pitch angles. Since optimal analysis settings are image-set dependent and generally unknown in advance, broader validation using diverse image-sets and non-optimal SfM settings is necessary.

Intrinsic camera parameters - such as focal length (f), principal point coordinates (c_x , c_y), radial distortion, tangential distortion - can be estimated during the bundle adjustment (BA) stage in a typical SfM pipeline (self-calibration), or alternatively, calculated using imagery captured specially for calibration purposes (pre-calibration). However, in UAV-based photogrammetry, where lightweight and compact drones with small cameras are commonly used, pre-calibrated intrinsic parameters are often considered unstable [25–28]. This instability can arise from mechanical effects during camera shooting, changes in image sensor temperature [19,29,30] or ambient temperature [31] during drone operations, potentially affecting the sensor geometry. Therefore, self-calibration has become the preferred approach for estimating these intrinsic parameters.

SfM using images captured by CPA flight design has been reported to perform well when the camera positions measured by RTK-GNSS are incorporated in BA [20,22]. However, when camera position measurements are unavailable, referred to as image-based SfM, the performance of SfM becomes notably unstable. Sanz-Ablanedo et al. [19] reported poor image-based SfM performance using CP flight images captured at 25° pitch angle, highlighting non-linear deformation (dome effect). Their study also noted large mean vertical errors at validation points located at the four corners of the model, which can be caused by inaccuracy in the estimation of focal length (f). Similarly, Kon et al. [32] reported dome errors accompanied with large RMS errors of all validation points, and in

some cases, alignment failures, across various SfM analysis settings (1500 trials) for images captured by CPA flights at 20° pitch angle. For these 1500 SfM trials, the standard deviation of f and c_y were notably large, 209 pixels and 84 pixels for camera Phantom 4 RTK drone, and 53 pixels and 36 pixels for camera SONY $\alpha 7$ III drone, respectively (unpublished). Observations of large mean vertical errors at validation points and alignment failures, coupled with the instability in estimations of f and c_y , suggest that factors beyond the dome effect may contribute to poor performance of image-based SfM. Despite these observations, the root causes of this instability have not been thoroughly investigated.

It has been mathematically shown that certain combinations of camera motion and scene geometry, known as critical configurations, can introduce indeterminacy into the bundle adjustment with self-calibration [33]. This study hypothesizes that the instability in camera parameters observed in CPA-based image sets stems from such critical configurations, leading to inaccurate or even incorrect model reconstructions.

Cameras inherently introduce lens distortions, which are typically modeled during the SfM process using the Brown distortion model [34]. This model accounts for common distortion types, such as radial and decentering distortions, and assumes that the input images are distorted and have not undergone any internal geometric correction. However, many UAV-mounted cameras (e.g., Phantom 4 RTK) apply in-camera geometric corrections before exporting images in JPEG format [35]. When such pre-corrected images are subsequently processed using the Brown model, the estimated distortions may instead reflect compensations for the prior in-camera adjustments, rather than representing the true optical distortions. This mismatch can lead to additional inaccuracies and systematic errors in the SfM-derived outputs.

Empirical evidence shows that several digital elevation models (DEMs) generated through SfM photogrammetry using UAVs with parallel-viewing image acquisition exhibit broad-scale systematic deformations, such as dome or bowl effects [15,35,36]. The dome/bowl effects in DEMs tend to render them unsuitable for change detection and monitoring studies.

1.2. Objectives

This dissertation aims to examine the causes of indeterminacy and inaccuracy in intrinsic parameter estimation in UAV-based photogrammetry using Structure from Motion (SfM), and to explore strategies to address these issues. The specific research questions addressed in each chapter are as follows:

1. Robustness of SfM accuracy and precision against non-optimality in analysis settings (Chapter 3)
 - Does the robustness of camera pitch angles between 20° and 35°, as reported by Takata et

al. (2021), remain consistent across a broader more image-sets and under different non-optimal analysis settings?

- To what extent does the performance of SfM degrade when the analysis setting is not optimal?
2. Indeterminacy of camera intrinsic parameters in Structure from Motion using images from Constant-Pitch flight design (Chapter 4)
 - Which camera intrinsic parameters can be indeterminate in SfM with self-calibration using only images?
 - Under what combinations of camera motion and scene geometry does this indeterminacy arise and how it can be mitigated?
 - How does the indeterminacy of camera intrinsic parameters manifest in real-data UAV surveys and what are its practical implications?
 3. Impact of in-camera distortion correction on systematic deformation in UAV-based photogrammetry using Structure from Motion (Chapter 5)
 - Does in-camera distortion correction lead to systematic deformation – such as dome or bowl effect – in DEMs derived from SfM using UAV imagery?
 - If so, what remedies or processing strategies can be implemented to mitigate this deformation?

1.3. Thesis structure

This dissertation is organized into five chapters. The following paragraphs provide an overview of each chapter:

Chapter 1 introduces the background, objectives and the scope of the study, outlining the key topics addressed in the subsequent chapters.

Chapter 2 presents the theoretical foundation of UAV-based photogrammetry using SfM. It covers the principles of SfM processing, analysis settings used in SfM software, intrinsic parameter estimation, overview of UAV flight design, and the role of in-camera distortion correction.

Chapter 3 examines the robustness of SfM accuracy and precision using 15 image sets and 750 different analysis settings. The images were acquired over relatively flat terrain using CPA-2D-GP flight design. The accuracy and precision of SfM is evaluated through the root mean square (RMS) error of all validation points. In addition, the correlation between estimated f and mean vertical error of all validation points is also analyzed.

Chapter 4 investigates the indeterminacy of intrinsic parameters in SfM using images from CPA-1D-GP flight design. The indeterminacy of two basic intrinsic parameters f and c_y is

examined in numerical experiments and validated using real-data captured at three ground sample distances (GSDs). A practical strategy for mitigating this indeterminacy is also proposed.

Chapter 5 addresses the inaccuracy of intrinsic parameters estimation resulting from in-camera distortion correction, applied before the SfM process, with a focus on its effect on systematic deformation in digital elevation models (DEMs). Three images acquired by CPA-2D-GP flight design are exploited to generate DEMs. The resulting deformations are assessed by comparing DEMs created from distortion-corrected and uncorrected images against reference DEMs.

1.4. Publications

Peer-reviewed Journal Paper

1. **Truc Thanh Ho**, Riku Sato, Ariyo Kanno, Tsuyoshi Imai, Koichi Yamamoto, Takaya Higuchi. (2025). Indeterminacy of camera intrinsic parameters in structure from motion using images from constant-pitch flight design. *Remote sensing*, 7(12), 2030. <https://doi.org/10.3390/rs17122030> (Printed)

This manuscript is related to *chapter 4* of this dissertation.

2. **Truc Thanh Ho**, Ariyo Kanno, Yuji Matsuoka, Masahiko Sekine, Tsuyoshi Imai, Koichi Yamamoto, Takaya Higuchi. (2024). Robustness of structure from motion accuracy/precision against the non-optimality in analysis settings: case study in constant-pitch flight design. *IJAT*. Vol.18 No.5. pp. 621-631. doi: 10.20965/ijat.2024.p062 (Printed)

This article is related to *chapter 3* of this dissertation.

Conference presentation

Truc Thanh Ho, Ariyo Kanno, Masahiko Sekine, Tsuyoshi Imai, Koichi Yamamoto, Takaya Higuchi. (2023). Impact of in-camera distortion correction on systematic deformation in photogrammetry using Structure from Motion and Unmanned Aerial Vehicle: a case study in constant-pitch meandering flight design. Asian Conference on Remote Sensing (ACRS2023) October 30 – November 3, 2023. Taipei, Taiwan.

The content of this study is related to *chapter 5* of this dissertation.

The findings of this study were first presented at the Asian Conference on Remote Sensing (ACRS 2023). The study was subsequently presented at the National Scientific Conference on Advances in Civil Engineering, Architecture, Economy, and Technology 2024 (ACEAT 2024), where it underwent peer review and was published in Vietnamese in the conference proceedings:

Truc Thanh Ho, Ariyo Kanno, Masahiko Sekine, Tsuyoshi Imai, Koichi Yamamoto, Takaya Higuchi. (2024). Impact of in-camera distortion correction on systematic deformation in photogrammetry using Structure from Motion and Unmanned Aerial Vehicles. In Proceedings of the National Scientific Conference on Advances in Civil Engineering, Architecture, Economy, and Technology 2024 (ACEAT 2024), Volume 2 (pp. 980–989). Hanoi: Construction Publishing House. ISBN 978-604-82-8109-0.

Chapter 2. Fundamentals of UAV-based photogrammetry and Structure from Motion

2.1. UAV-based photogrammetry

Unmanned Aerial Vehicle (UAV)-based photogrammetry refers to the process of reconstructing three-dimensional (3D) scenes from two-dimensional (2D) images captured by UAVs. The image acquisition process involves projecting real-world 3D points onto a 2D image plane. The relationship is governed by a coordinate transformation (Fig. 2-1), from the world coordinate system to the image (pixel) coordinate system. This procedure generally involves two main steps:

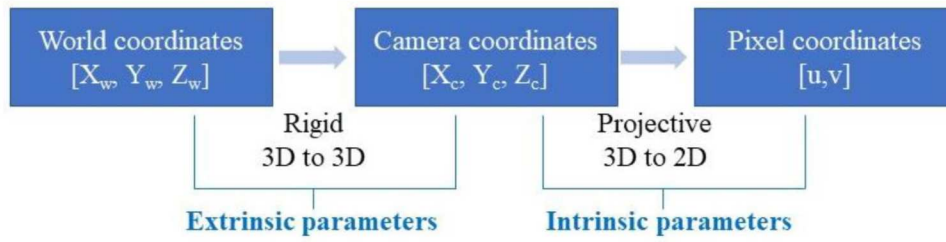


Figure 2-1. Coordinate transformation from 3D point to 2D.

a) *Transformation from world coordinate system to camera system:*

This step refers to a rigid body transformation that relates a point X (X_w, Y_w, Z_w) in the world coordinate system to a corresponding point X_c (X_c, Y_c, Z_c) in the camera coordinate system (Fig. 2-2). The transformation is performed using the Helmert transformation, which consists of:

- A rotation matrix R , representing the camera's orientation, and
- A translation vector t , representing the camera position relative to the world coordinate origin.

These parameters are collectively known as the camera extrinsic parameters, which describe the camera's pose (position and orientation) in 3D space.

This transformation can be mathematically expressed as:

$$\begin{bmatrix} X_c \\ Y_c \\ Z_c \end{bmatrix} = R \begin{bmatrix} X_w \\ Y_w \\ Z_w \end{bmatrix} + t \quad (2-1)$$

b) *Transformation from camera coordinate system to pixel coordinate system:*

In this step, the 3D point X_c (X_c, Y_c, Z_c) is projected onto 2D image plane and subsequently mapped to the pixel coordinate system, represented as (u,v) (Fig. 2-2). This projection is controlled by the camera *intrinsic parameters*, which describes the internal geometric characteristic of the camera.

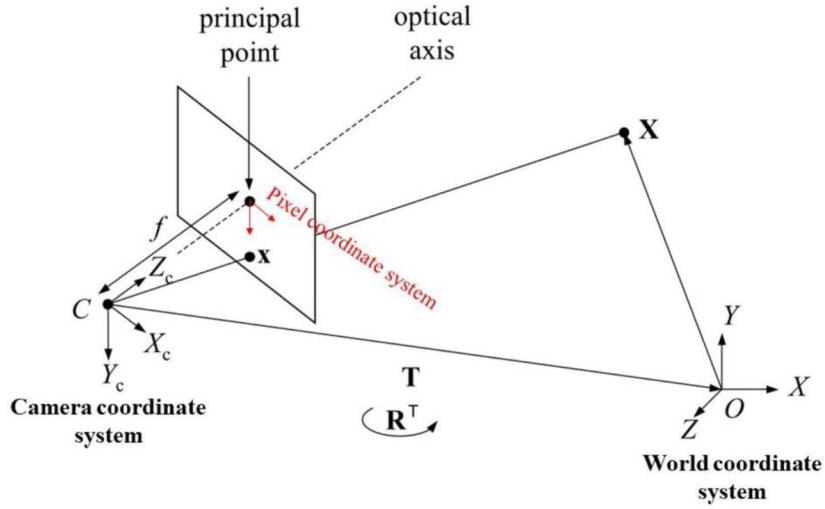


Figure 2-2. Pinhole projection of a 3D point X onto a camera image plane.

The normalized image coordinates on the image plane are defined as:

$$x = \frac{X_c}{Z_c}, y = \frac{Y_c}{Z_c} \quad (2-2)$$

The mapping from image plane coordinates to pixel coordinates is then expressed as:

$$\begin{bmatrix} u \\ v \end{bmatrix} = \begin{bmatrix} f_x & 0 & c_x \\ 0 & f_y & c_y \end{bmatrix} \begin{bmatrix} x \\ y \\ 1 \end{bmatrix} \quad (2-3)$$

Where: (u, v): the pixel coordinates of the projected point.

f_x, f_y : camera focal length (pixels).

c_x, c_y : coordinates of the principal point (pixels), which is the intersection of the optical axis with the image plane (Fig 2-2).

Equation 2-3 assumes an ideal pin hole camera model without any lens distortion.

2.2. Intrinsic parameters estimation

In photogrammetry, camera's intrinsic parameters describe camera's internal geometry and optical characteristics. These typically include the focal length (f), the principal point coordinates (cx, cy), and lens distortion coefficients that model optical distortions such as radial and tangential distortions.

2.2.1. Radial and tangential distortions.

✓ Radial distortion occurs when light rays bend more near the edges of a lens than at its optical center. This causes straight lines to appear curved, leading to effects like barrel or pincushion distortion (Fig 2-3). Radial distortion becomes more pronounced with smaller focal lengths (wide-angle lenses).

✓ Tangential distortion (Fig 2-4) arises when the lens is not parallel with the image plane. This misalignment causes the image points to shift tangentially, resulting in asymmetric deformation of the image geometry. Such effects are modeled using tangential distortion coefficients.

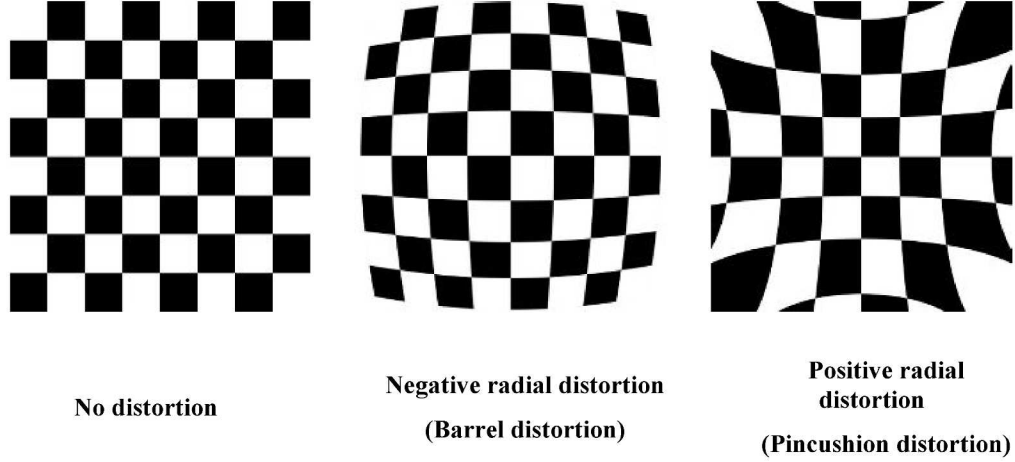


Figure 2-3. Effect of radial distortion on a square grid.

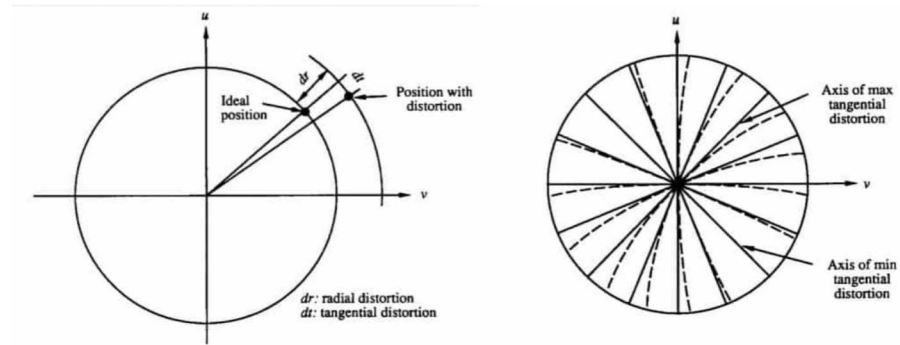


Figure 2-4. Effect of tangential distortion. The solid lines represent case of no distortion and dashed lines are with tangential distortion (right) and (left) how tangential and radial distortion shifts a pixel from its ideal position.

2.2.2. Brown-Conrady distortion model

To mathematically describe these distortions, the 2D image coordinates initially are normalized as follows:

$$x = \frac{X_c}{Z_c}, y = \frac{Y_c}{Z_c},$$

$$r = \sqrt{x^2 + y^2}$$
(2-4)

The distorted image coordinates (x' , y') are then calculated using the Brown-Conrady distortion model (Brown model) [37]:

$$x' = x (1 + k_1 r^2 + k_2 r^4 + k_3 r^6 + k_4 r^8) + [p_1(r^2 + 2x^2) + 2p_2 xy]$$
(2-5)

$$y' = y (1 + k_1 r^2 + k_2 r^4 + k_3 r^6 + k_4 r^8) + [p_2(r^2 + 2y^2) + 2p_1 xy] \quad (2-6)$$

The final pixel coordinates (u, v) of projected points are obtained by applying intrinsic parameters. For instance, in Agisoft Metashape v2, the mapping is expressed as:

$$u = w * 0.5 + c_x + x'f + x'b_1 + y'b_2 \quad (2-7)$$

$$v = h * 0.5 + c_y + y'f \quad (2-8)$$

Where:

- (w, h): image width and height (in pixels)
- k_1, k_2, k_3, k_4 : radial distortion coefficients
- p_1, p_2 : tangential distortion coefficients
- b_1, b_2 : skew coefficients (often negligible or zero)

The Brown model assumes that distortions are physically introduced by the lens and thus can be modeled and corrected accordingly. However, in some consumer-grade UAV cameras, distortion corrections are automatically applied before the image is saved in JPEG format - prior to any photogrammetric processing [35]. These in-camera corrections typically aim to:

- + Reduce the visual geometric artifacts (e.g. straight lines appearing curved), primarily caused by radial distortion.
- + Enhance image appearance through color adjustments, sharpening, or contrast enhancement.

While these corrections may improve image aesthetics, they often do not conform to the Brown model. As a result, processing pre-corrected images using the Brown model can introduce inconsistencies and systematic errors in the estimation of intrinsic parameters during SfM processing.

2.3. Structure from Motion

Structure from Motion (SfM) is the key technique in UAV-based photogrammetry. It enables the simultaneous estimation of scene structure and camera intrinsic and extrinsic parameters from a set of overlapping 2D images. The image capture process is modeled as a 3D-to-2D projection using the mathematical transformations introduced in Equations (2-1) and (2-2) from Section 2.1. The goal of SfM is to estimate the following parameters simultaneously:

- Extrinsic parameters: define the relative position and the orientation of each camera.
- Intrinsic parameters: represent the geometric characteristics of the camera, such as focal length, principal points and distortion coefficients.
- 3D point coordinates: the relative spatial coordinates of scene points in object space, reconstructed from multiple views.

The process of SfM with self-calibration is illustrated in Fig 2-5, which outlines the general workflow of UAV-based photogrammetry for generating a dense point cloud.

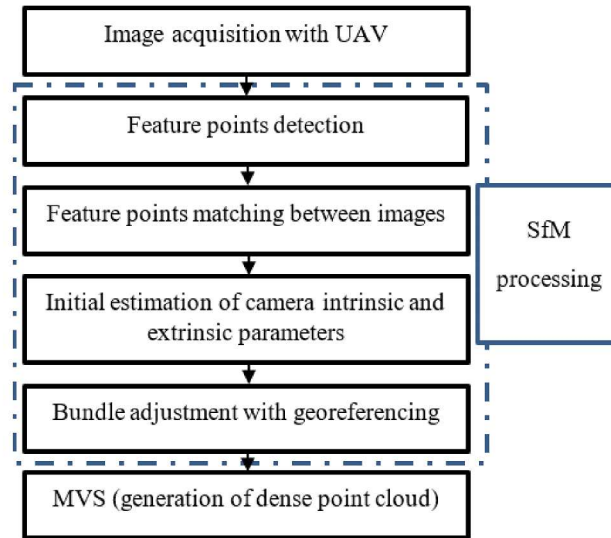


Figure 2-5. UAV SfM-photogrammetry workflow for generating a dense point cloud.

SfM has gained popularity in recent years due to its capability to reconstruct 3D models from unordered and heterogeneous images, without prior knowledge of the camera parameters [30]. It differs from traditional photogrammetry in three main aspects:

- (i) Automatic feature matching: image features can be detected and matched across variations in scale, orientation and viewpoint, which is particularly useful for images captured from small, unstable platforms;
- (ii) No prior geolocation required: SfM can operate without known camera positions or GCPs to estimate camera parameters, although this auxiliary information can be integrated to enhance accuracy.
- (iii) Automatic camera calibration: intrinsic and extrinsic parameters can be estimated and refined automatically during the SfM process as self-calibration, without the need for dedicated calibration procedures (pre-calibration).

Full details of different steps of the SfM-MVS workflow can be found in Lowe (2004), Snavely et al. (2008), and James and Robson (2012) [38–40]. The standard SfM procedure consists of three main steps:

1. Feature point extraction

Distinctive image features (keypoints), represented by pixel coordinates (u_d , v_d) are detected in each image. These features are invariant to changes in scale, rotation, and illumination changes.

2. Feature point matching

Corresponding feature points are matched between overlapping images by comparing their descriptors. Each matched pair is assumed to represent the 2D projections of the same 3D point in the scene.

3. Bundle adjustment (BA)

Once feature correspondences are established, the extrinsic and intrinsic camera parameters, along with the 3D coordinates of the matched points, are jointly estimated and refined through bundle adjustment (BA). This process minimizes the overall reprojection error (Fig 2-6), defined as the difference between the projected point (u_c, v_c) (computed from the estimated 3D model and parameters) and the observed feature location (u_d, v_d) (detected in the image).

$$\text{Reprojection error} = (u_c, v_c) - (u_d, v_d)$$

The objective function in SfM is expressed as the root mean square (RMS) of all reprojection errors:

$$\text{Objective function} = \text{RMS of all reprojection errors}$$

For successful camera estimation, this objective function must have a unique global minimum. If multiple minima exist, the optimization algorithm may converge to an incorrect solution, leading to reconstruction failure.

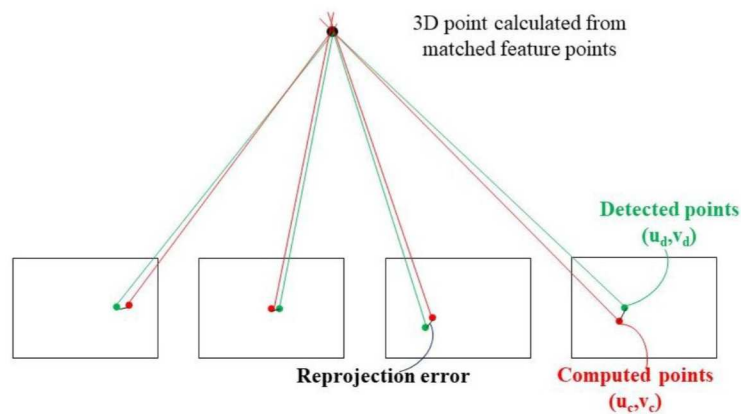


Figure 2-6. Reprojection error calculation

Use of auxiliary constraints

In some cases, additional constraints can be incorporated into the bundle adjustment to improve the estimation of camera parameters. For example, when camera's position at the moment of image capture is recorded using an onboard RTK-GNSS receiver, an additional error (RTK-GNSS error) can be added to the objective function to represent the discrepancy between the estimated and measured camera positions:

$$\text{Objective function} = \text{RMS of reprojection errors} + \text{RMS of RTK-GNSS errors}$$

While this integration of such geolocation data can significantly improve the accuracy of parameter estimation, but it also increases the complexity, cost, and time required for data collection.

Validation points

After the successful estimation of camera parameters through SfM, additional ground points - not used in the original feature matching or BA process - can be reconstructed by triangulation using the

known camera parameters. These are referred to as validation points.

The process is similar to bundle adjustment, with two key differences:

- The camera parameters are fixed, having already been estimated in the previous steps.
- Only the 3D coordinates of the new points are optimized.

This technique is commonly employed to evaluate the accuracy and precision of the SfM output. The estimated 3D coordinates of validation points are compared with their ground-truth coordinates obtained from static GNSS surveys. The RMS error between the estimated and measured coordinates is computed as:

Validation point error = RMS of differences between estimated and measured coordinates of validation points

2.4. UAV flight design

One of the critical factors influencing the accuracy and precision of UAV-based photogrammetry using SfM is the flight design, particularly the image acquisition pattern. A well-designed flight plan can enhance camera parameters estimation and improve the overall quality of SfM outputs [9,16,17]. Consequently, various UAV flight strategies have been investigated to optimize 3D reconstruction performance.

Constant-Pitch-Angle (CPA) flight patterns are widely employed image acquisition method in UAV-based photogrammetry [18–22,32,41]. In these flight designs, the camera maintains a fixed pitch angle along the flight lines, and the optical axes of the images within the same strip are parallel. When the UAV flies in opposing direction, local image convergence is achieved, that facilitates 3D reconstruction.

Two commonly used CPA configurations are:

- CPA-2D-GP: Constant-Pitch-Angle, Two-Directional, and Gridded-Position
- CPA-1D-GP: Constant-Pitch-Angle, One-Directional, and Gridded-Position

In CPA-2D-GP flight design (Fig 2.7a), the UAV flies in two directions and includes intermediate strips placed orthogonally between adjacent flight lines. In contrast, CPA-1D-GP (Fig 2.7b) involves flight in a single direction per strip, without intermediate strips. CPA-1D-GP mission can be created using built-in mission planning tools such as Pix4Dcapture.

CPA-based flights - especially with 0° pitch angle – have been shown to result in poor performance and low consistency in SfM [10,15,36]. These limitations arise primarily because camera viewing directions parallel to the ground make it difficult or impossible to accurately estimate key intrinsic parameters, particularly the focal length (f).

Other image acquisition patterns have demonstrated significantly better performance. For instance, Sanz-Ablanedo et al. (2020) [17] showed that Point of Interest (POI) flight, where all camera

orientations converge toward the center of the survey area, achieved the highest accuracy with minimal dome errors (less than 0.25 m), due to strong image network geometry. Similarly, James et al. (2014) [36] demonstrated that including oblique images in the acquisition plan significantly reduces DEM error, even without using control points.

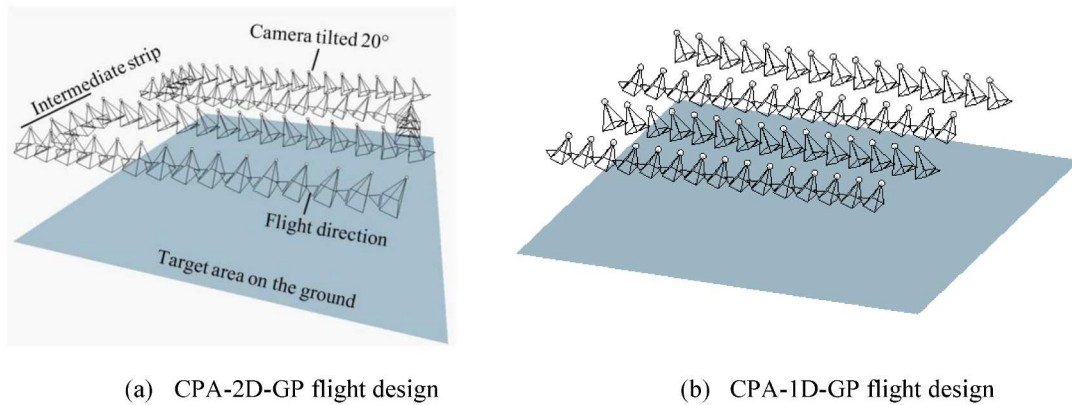


Figure 2-7. CPA-2D-GP and CPA-1D-GP flight design at 20° pitch angle.

Beyond the above flight patterns, several other mission types are used to meet different mapping objectives:

- Double grid flight: Combines two CPA-1D-GP flights flown in opposite directions. This pattern increases image overlap and directional variation, improving model stability and reducing systematic errors.
- Corridor mission: designed for linear features such as roads, rivers, or pipelines. The camera alignment and spacing are optimized for narrow, elongated areas.
- Waypoint (custom) missions: provide flexible image acquisition by allowing surveyors to manually set flight paths, camera angles, and intervals.

2.5. Analysis settings in SfM

The accuracy and precision of UAV-based photogrammetry using SfM is highly influenced by the analysis settings used in photogrammetric software. These settings control feature detection, matching, and bundle adjustment, which in turn affect the estimation of camera parameters and 3D point coordinates. This section provides an overview of the key analysis settings in Agisoft Metashape version 1.5.5, categorized into three main groups: align photos, reference settings, and optimize camera alignment.

2.5.1. Align photos

This group of settings governs the initial feature extraction and image alignment process.

- Accuracy: controls the size of the input images used for feature extraction.

Setting values: High, Medium

The “High” accuracy setting uses the original images.

The “Medium” accuracy setting causes images downscaling by factor of 4 (two times by each side).

Higher accuracy settings help to obtain more accurate camera position estimates but longer processing time.

- Key point limit: specifies the maximum number of feature points (keypoints) detected in each image.

Setting values: the standard settings is 50,000 per image. In this study, values equivalent to 1/2, 1/3, 1/4 of the average detectable key points were tested.

- Tie point limit: sets the maximum number of tie points (matched key points across images) retained for each image after feature matching.

A value of 0 disables any filtering and retains all tie points.

2.5.2. Reference settings

These parameters specify the weighting of image and tie point positions in the objective function of bundle adjustment, especially when external reference data (e.g., RTK-GNSS or GCPs) is used.

- Camera accuracy

Sets the weight attributed to the camera position data (e.g., RTK-GNSS or GCPs) in bundle adjustment.

Setting values: 0.25, 0.5, 1, 2, 4 times the camera position precision embedded in each image.

Higher values indicate greater trust in externally measured camera positions.

- Tie point accuracy

Sets the weight for the accuracy of tie points position in bundle adjustment.

Setting values: 0.25, 0.5, 1, 2, 4 times the default tie point accuracy (1) in pixel.

This corresponds to positional uncertainties ranging from 0.25 to 4 pixels.

2.5.3. Optimize camera alignment

This setting determines which intrinsic camera parameters are estimated and optimized during bundle adjustment. The optimization is based on the Brown distortion model, which includes both radial and tangential distortion parameters, along with focal length, principal point, and optional skew parameters.

Various combinations of parameters can be selected, depending on assumptions about the camera model and distortion characteristics.

Setting values:

- f, cx, cy, k1–k4, p1–p4, b1, b2
- f, cx, cy, k1–k4, p1–p4

- $f, cx, cy, k1-k4, p1-p2$
- $f, cx, cy, k1-k3, p1-p4$
- $f, cx, cy, k1-k3, p1-p2$: commonly used as the standard setting.

Where:

f : focal length

cx, cy : principal point coordinates

$k1 - k4$: radial distortion coefficients

$p1 - p4$: tangential distortion coefficients

$b1, b2$: skew coefficients (usually negligible)

Chapter 3. Robustness of SfM accuracy and precision against non-optimality in analysis settings

3.1. Introduction

The accuracy and precision of UAVs - based photogrammetry that employs Structure from Motion and Multi-View Stereo (SfM-MVS) can be affected by several factors, including the analysis settings used in the SfM process. In this study, the robustness of SfM accuracy and precision against the non-optimal analysis settings was evaluated by performing 750 different analysis settings of SfM on 15 image-sets captured at five distinct pitch angles and three distinct ground sample distances (GSDs).

All flights were conducted over a 100 x 100 m² flat surface using the Constant-Pitch-Angle, Two-Directional, and Gridded-Position flight design (CPA-2D-GP) flight design (Fig 2-7a). Camera coordinates measured by RTK-GNSS were integrated into the bundle adjustment (BA) during SfM and georeferencing. The accuracy and precision of SfM were evaluated using nine validation points distributed evenly across the target area.

3.2. Methods

3.2.1. Data acquisition

Experiments were conducted to capture a flat 100 x 100 m² area, constructed for housing purposes, in Tsukubamirai City, Ibaraki Prefecture, Japan, to capture a flat 100 m × 100 m area. Fig. 3-2 shows the ground conditions, which are mostly bare land partly covered with short vegetation types. The meteorological conditions listed in Table 3-1 were recorded at Tsukuba weather station during the flight.

Table 3-1. Meteorological conditions during image acquisition

Ground sample distance (mm)	GSD20	GSD15	GSD10
Date of data acquisition	21 st July 2020		
Time of day	11:03–11:41	13:39–14:23	14:33–15:28
Site dimension (m ²)	100	100	100
Solar radiation (MJ/m ² /day)	1.1	1.33 – 1.44	1.2 – 1.44
Wind speed (m/s)	5	3	2.8
Weather condition	Cloudy	Cloudy	Cloudy

Aerial photographs were collected using a high-precision 1-inch 20 MP CMOS camera sensor attached to a lightweight quadcopter UAV (DJI Phantom 4 RTK; hereafter named P4RTK). The assembled camera lens had an actual focal length of 8.8 mm and a mechanical shutter feature that

avoided typical rolling shutter problems. This UAV embeds an RTK-GNSS to produce a highly accurate camera position during the exposure time. During image acquisition, the UAV can either stop for each shot or capture images while moving for efficiency.

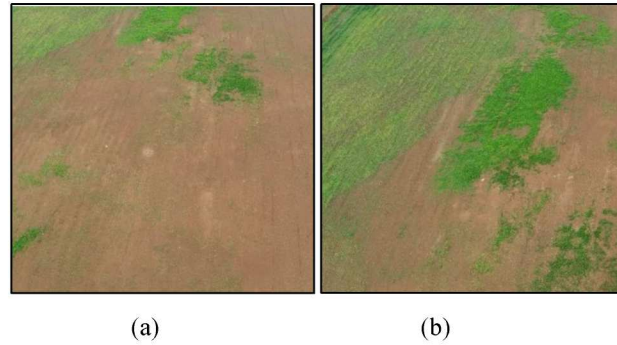


Figure 3-1. Actual terrain situation captured by pitch angle of 40° of GSD15 for bare land (a) and vegetation covering area (b).

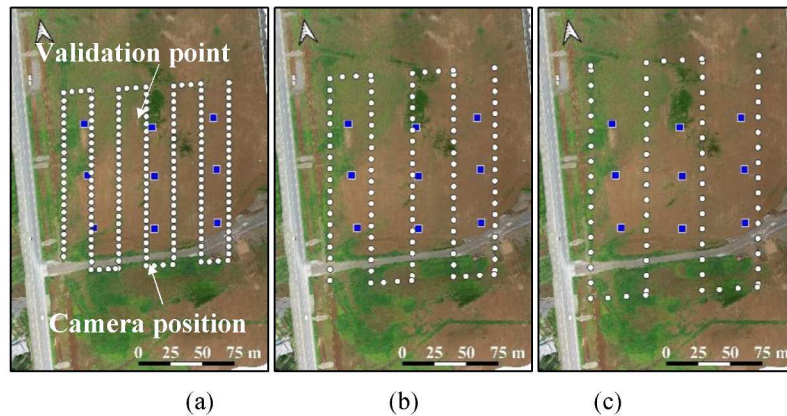


Figure 3-2. Distribution of camera positions and validation points at the study site overlaid with orthophotos generated by GSD 10 (a), GSD 15 (b), and GSD 20 (c).

At each validation point, world coordinates were measured by Aerobo markers with a built-in GNSS receiver.

A Constant-Pitch-Angle, Two-Directional, and Gridded-Position flight design (CPA-2D-GP) was used for data acquisition. The flight design was generated using a 3D photogrammetry preset feature in the P4RTK system. On specifying the flight altitude and overlap ratio, the 3D photogrammetry module automatically generates the flight route, captures images at two-second intervals, and records camera coordinates using RTK-GNSS at the time of image capture. In this study, P4RTK was flown at altitudes of 73, 55, and 36 m above ground level (at the drone's home point), yielding three GSDs of 20, 15, and 10 mm. All photographs captured from parallel flight lines achieved the same overlap ratio of 80% forward and 60% side lap when the optical axis of the camera was at the heading nadir. This overlap ratio is typically used for the UAV data collection [42,43]. Fig. 3-2 shows the geometry and corresponding image strips yielded at each GSD when the camera was tilted by a fixed pitch along the flight courses of 0°, 10°, 20°, 30°, and 40°. Table 3-2 lists the parameters of the individual

flights with the designation and number of images used.

Validation points

A set of nine validation points was employed to evaluate the accuracy of SfM performance using the AeroBo marker. These points were uniformly distributed across the study site (Fig. 3-2) and functioned as fixed reference points. With a built-in GNSS receiver, AeroBo markers collect the coordinates of the validation points positioned at the centers of circular black-and-red markers (with a diameter of 0.24 m) with sub-centimeter accuracy. Their red-black reflection color enables automatic detection by SfM processing software [44].

Table 3-2. Summary of the 15 flights used in this study.

Image set	Pitch angle [°]	Number of images	Shooting attitude [m]	Overlap ratio [%]
1	0	57	73 (GSD 20)	80% forward, 60% side lap.
2	10	65		
3	20	73		
4	30	80		
5	40	92		
6	0	87	55 (GSD 15)	
7	10	97		
8	20	107		
9	30	117		
10	40	132		
11	0	166	36 (GSD 10)	
12	10	174		
13	20	187		
14	30	207		
15	40	222		

3.2.2. SfM processing

For each image set acquired by P4RTK, SfM was performed using the commercial software package Agisoft Metashape version 1.5.5. The procedure of SfM is illustrated in Fig. 2-5, known as “align photos” in Metashape software. In this process, the projection centers recorded by RTK-GNSS embedded in the images taken by P4RTK were used for both bundle adjustment and georeferencing processing.

In this study, SfM focused only on self-calibration, where the internal camera parameters were estimated using SfM. This is because the camera attached to the drone is of consumer grade, and the intrinsic parameters of such cameras are generally not considered stable [45].

The absolute coordinates of the validation points evaluated by multi-view triangulation using the camera parameters estimated in SfM were used to validate the accuracy of the SfM-derived model.

The robustness of SfM was tested using a combination of the analysis settings summarized in Table 3-3. This resulted in 750 analysis settings, with two trials for each image set. The analysis settings considered here are the fundamental components commonly processed in most SfM-based software, including Metashape.

In Table 3-3, the input image quality for SfM process excluded “low image size” (downscaled original image size by a factor of four for each size) because it naturally resulted in insufficient number of feature points, leading to an unstable SfM process.

Table 3-3. Summary of the analysis settings tested in this study.

Setting items	Meaning - Setting values
Align photos	
Accuracy	<ul style="list-style-type: none"> ✓ Set the size of input images for feature extraction. High: original size Medium: image downscaled by a factor of two at each image side. ✓ Setting values: High, medium
Key point limit	<ul style="list-style-type: none"> ✓ Set the maximum number of feature points detected in each image. ✓ Setting values: 1/2, 1/3, 1/4 of the average number of detectable keypoints for the input images, corresponding to: <ul style="list-style-type: none"> • 35643, 23762, 17821 when Align photos Accuracy is set as High. • 8229, 5486, 4115 when Align photos Accuracy is set as Medium.
Tie point limit	<ul style="list-style-type: none"> ✓ Set the maximum number of tie points to be detected in each image. ✓ If it is set to 0, it will attempt to detect as many tiepoints as possible in each image. ✓ Setting values: 0
Reference settings	
Camera accuracy	<ul style="list-style-type: none"> ✓ Set the weight attributed to the image position in bundle adjustment. ✓ Setting values: 0.25, 0.5, 1, 2, 4 times of the camera position precision embedded in each image.
Tie point accuracy	<ul style="list-style-type: none"> ✓ Set the weight attributed to tie point position in bundle adjustment. ✓ Setting values: 0.25, 0.5, 1, 2, 4 times of the default tie point accuracy (1) in pixel, corresponding to 0.25, 0.5, 1, 2, 4 pixels.
Optimize camera alignment	
	<ul style="list-style-type: none"> ✓ Select the camera intrinsic parameters for optimization. ✓ Setting values: <ol style="list-style-type: none"> ① f, cx, cy, k1-k4, p1-p4, b1, b2 ② f, cx, cy, k1-k4, p1-p4 ③ f, cx, cy, k1-k4, p1-p2 ④ f, cx, cy, k1-k3, p1-p4 ⑤ f, cx, cy, k1-k3, p1-p2
750 analysis settings with 2 trials, equivalent to 1500 trials for each image set.	

To assess the influence of camera intrinsic parameter estimation on the accuracy of SfM, five camera models (1–5; Table 3-3) were tested. These camera models differ in the absence or presence of high-order radial distortions (k4), tangential distortions (p3 and p4), and pixel distortions (b1 and b2).

3.2.3. Error evaluation and comparison

The accuracy and precision of the SfM were evaluated by calculating the root mean square (RMS) error of all nine validation points for each analysis setting, as recommended by James et al.[46]. The validation point error represents the difference between the two estimated 3D coordinates of the validation points (calculated through triangulation using camera parameters estimated during the SfM process) and those obtained through static GNSS positioning (Aerobo markers). Moreover, we

calculated the maximum (100th percentile value), 95th percentile, 75th percentile (Q3), median, and 25th percentile (Q1) values of the RMS errors of all the validation points for the 750 settings (with two trials for each setting). They were then used to quantify and interpret the robustness of the accuracy and precision of the SfM. The interquartile range (IQR) of the focal length f and RMS error of the validation points were used to quantify the spread or dispersion of these values within the 750 tested SfM analysis settings.

Additionally, the mean vertical error for all the nine validation points was evaluated in each analysis setting. The mean vertical error (MEZ) was defined as the average difference between the elevation of the estimated validation points (derived using camera parameters estimated by SfM) and the corresponding validation points measured by the AeroBo markers.

Subsequently, the vertical error rate was determined as the percentage of the absolute value of the mean vertical error of all the validation points to the RMS error of all the validation points. The mean vertical error rate was then calculated as the median value across 750 SfM settings (two trials for each setting).

3.2.4. Alignment failure and valid matching tallying

To understand the correlation between the RMS error of all validation points and pose estimation by SfM, we calculated the alignment failure rate and the number of valid matches for the images in the main strips (denoted as ST in Fig.3-3). The main strip is an image strip containing consecutive images captured along the flight line with a yaw angle deviation of no more than 5°. Additionally, four images captured during the drone rotation (between the two main strips) are referred to as intermediate strips.

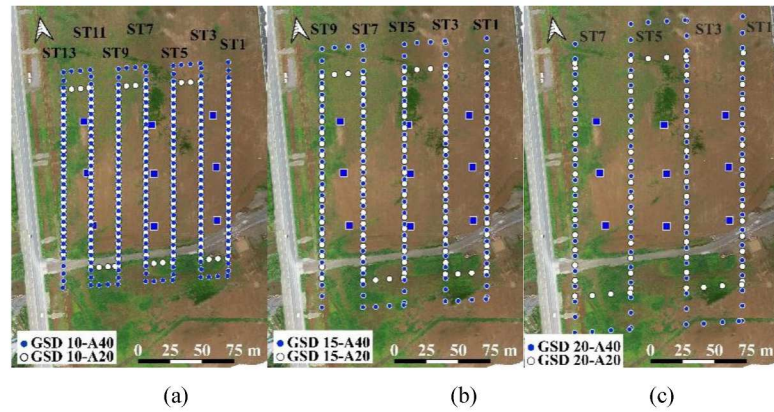


Figure 3-3. Main strip (named as ST) in images.

Blue color refers to camera positions of image sets taken at a pitch angle of 40°, and white color refers to a pitch angle of 20°. (a) GSD 10; (b) GSD 15; (c) GSD 20.

The feature points in the two images were geometrically matched through valid matching during

alignment and used to create 3D points. The number of valid matches for each main-strip was tallied in terms of **intra-strip** and adjacent inter-strip matching. **Intra-strip matching** refers to the matching of images located within the same strip, whereas adjacent inter-strip matching refers to the matching of images of the candidate strip with adjacent strips.

Valid matching tallying was performed for one alignment setting (alignment photo accuracy set as medium, keypoint limit of 1/3).

In addition, the alignment failure rate was defined as the percentage of images within an image set that failed to obtain the extrinsic camera parameters estimated relative to the total number of images in that image set. This rate is presented as an average value across 1500 trials for each image set.

3.3. Results

The results are divided into four sections. The first section presents the SfM accuracy and precision for image sets with a 0° pitch angle (parallel-axes direction). Subsequently, the robustness of the SfM accuracy and precision against non-optimal analysis settings is shown for datasets with pitch angles of 10° , 20° , 30° , and 40° using the RMS error of all validation points. In the third section, we assess the correlation between the mean vertical error of all the validation points and the intrinsic parameters estimated using SfM. The fourth section delves into the investigation alignment failures and their correlation with the number of valid matchings.

3.3.1. SfM accuracy and precision for image-sets taken at 0° pitch angle.

Out of 1500 trials, complete failure of SfM alignment for all images in the image-sets taken at a 0° pitch angle was observed in two trials of GSD15 and one trial of GSD20.

As shown in Table 3-4, RMS error of all validation points was significantly large, with an interquartile range of 35.7 m in GSD10 and 53.4, 72.2 m in GSD15, GSD20, respectively, after excluding trials with complete failure of SfM alignment. Furthermore, the alignment failure rate of the image sets captured at this pitch angle was greater than 9.6% (GSD20). These results demonstrate that SfM for image sets obtained at a 0° pitch angle is highly unstable and inaccurate.

Consequently, we excluded these 0° pitch-angle flights from further discussion.

3.3.2. Robustness of SfM accuracy and precision against non-optimal SfM analysis settings.

Table 3-5 summarizes the statistics of the RMS error of all the validation points for the 750 SfM analysis settings for each image set (taken from a 10° to 40° pitch angle). Although the RMS error of all validation points varies with the image set and analysis setting, our results show that the SfM analysis settings consistently yielded relatively small RMS errors for the validation points in some cases.

Table 3-4. Statistics of RMS error of all validation points for 0° pitch angle image-sets
(750 analysis settings with 2 trials of each setting)

Ground sample distance [mm]	Statistic of RMS error of all validation points [m]				Alignment failure rate [%]
	Q1	Q2	Q3	Interquartile range (IQR)	
GSD 10	0.041	0.069	35.298	35.678	26.257
GSD 15	0.084	0.334	53.618	53.421	29.649
GSD 20	0.138	0.334	69.848	72.198	9.615

Specifically, the results demonstrate that 100% and 95% of the SfM analysis settings for image sets taken at a 20° pitch angle yielded relatively small RMS errors of validation points, which is less than 0.056 and 0.048 m (corresponding to 2.8 and 2.4 times of GSD), respectively. Similarly, for image sets captured at a 30° pitch angle, all 750 analysis settings of SfM resulted in an RMS error of all validation points of less than 0.046 m (corresponding to 3.1 times the GSD). These levels of accuracy and precision were comparable to those of the RTK-GNSS measurements.

However, the RMS error of all validation points was large in the image sets captured at 10° (reaching values of 0.298 m) and 40° pitch angles, as shown in Table 3-5. Notably, 95% of the analysis settings in image sets with a 40° pitch angle achieved exceptional accuracy, with an RMS error of all validation points at 0.034 m. However, certain settings resulted in an extremely large RMS error of all validation points.

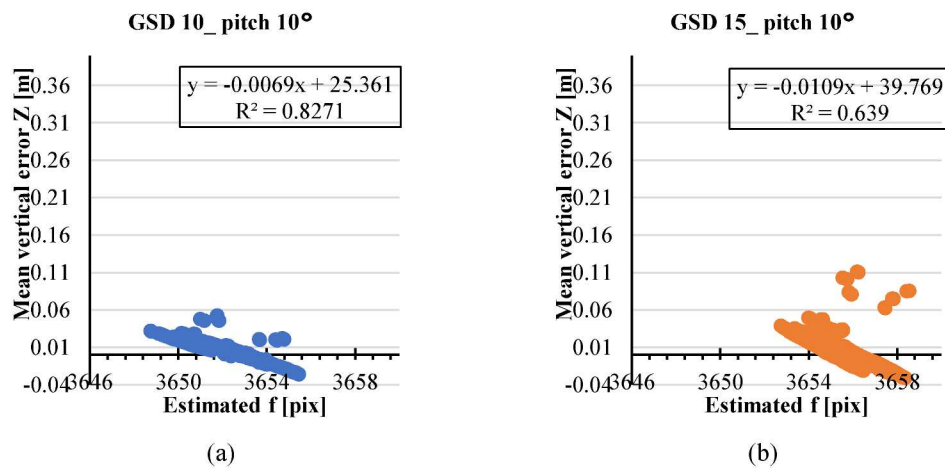
Overall, these results demonstrate that the SfM accuracy and precision are robust against 750 SfM analysis settings when shooting at 20° and 30° pitch angles. However, when shooting at 10° and 40° pitches, the accuracy and precision of SfM varied depending on the SfM analysis settings.

Table 3-5. Statistics of RMS error of all validation points and intrinsic parameters for each image-set (750 analysis settings with 2 trials of each setting)

Ground sample distance [mm]	Pitch Angle [°]	Interquartile range of f [pix]	Statistic of RMS error of all validation points [m]				Mean vertical error rate [%]	Alignment failure rate [%]
			Median	Interquartile range	95th percentile value	Maximum value		
GSD 10	10	2.045	0.027	0.002	0.035	0.089	24.7	0.025
	20	1.418	0.024	0.001	0.026	0.037	7.4	0
	30	1.004	0.025	0.001	0.027	0.029	38.0	0
	40	1.399	0.030	0.001	0.032	0.033	44.5	0
GSD 15	10	1.910	0.027	0.004	0.039	0.153	5.7	0
	20	1.537	0.022	0.001	0.026	0.046	12.9	0
	30	1.057	0.023	0.001	0.026	0.028	61.1	0
	40	1.364	0.030	0.002	0.035	0.037	62.4	0.382
GSD 20	10	2.483	0.066	0.021	0.118	0.298	90.6	0
	20	0.946	0.037	0.005	0.048	0.056	61.9	0
	30	1.218	0.027	0.001	0.031	0.036	20.8	0
	40	1.244	0.022	0.002	0.034	>10 ¹¹	0.6	10.732

3.3.3. Correlation between the mean vertical error of all validation points and the estimated intrinsic parameters.

As summarized in Table 3-5, the image sets taken with a 10° pitch angle suffered from larger RMS errors of all validation points (reaching 0.298 m) and a greater variation in the estimated f (observed in the interquartile range value in the 3rd column) compared to those of other pitch angles. To comprehend this phenomenon, a correlation analysis was employed to examine the relationship between the mean vertical error of all validation points (MEZ) and the estimated intrinsic parameter (focal length f). As illustrated in Fig 3-4, the results demonstrate a negative correlation between the estimated focal length f and the MEZ for most image sets taken with a 10° pitch angle. This outcome is natural for a pinhole camera model because, as the estimated f increases, the triangulated ground points move further from the cameras, and consequently, their estimated vertical coordinates decrease. However, owing to the possible correlations between f and other camera parameters, this was not the case for image set named “GSD 20_pitch 10°.” As shown in Fig 3-4 (c), the points are aligned on two “positive correlation” lines, in addition to the main “negative correlation” line. Although further details are not within the scope of this study, these three lines are characterized by different SfM settings and different resultant correlations among the intrinsic parameters. Additionally, the image-set “GSD 20_pitch 10°” exhibited a mean vertical error rate of 90.6%, suggesting vertical error to be the main contributor to the total RMS error of all validation points. These results indicate that the inconsistencies in estimating f (for the 750 SfM settings of each image set) are likely the driving factors causing the large RMS error of all validation points when shooting at a 10° pitch angle.



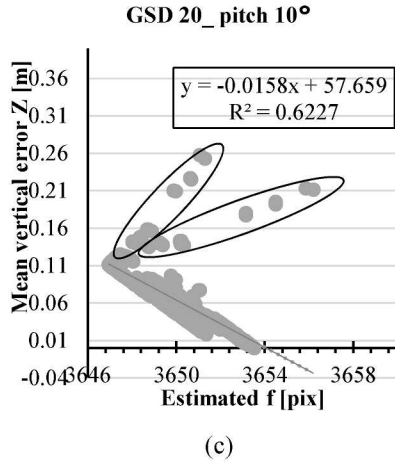


Figure 3-4. Correlation between the mean vertical error of all validation points (MEZ) and estimated f in image-sets of 10° pitch angle (a) GSD 10; (b) GSD 15; (c) GSD 20

Moreover, for the image sets of GSD20, as the camera inclination increased from 10° to 40°, the mean vertical error rate decreased substantially (8th column of Table 3-5). However, owing to the small RMS error of all the validation points (less than 0.046 m) obtained in the image sets of GSD 15 and GSD 10 for pitch angles ranging from 20° to 40°, which are comparable to the RTK-GNSS accuracy, the correlation between the vertical error rate and pitch angle might not be evident.

3.3.4. Alignment failure and valid matching

To investigate the cause of the significant variability in the RMS error of all validation points observed in the image sets captured at a 40° pitch angle, we examined both the alignment failure rate and quantity of valid matchings. I used image sets with a 20° pitch angle as a benchmark for comparison, because they were robust in the various analysis settings that we tested. Valid matching was tallied for the main strips, including adjacent inter-strip matching and **intra-strip matching**. The ratio of adjacent inter-strip matching to intra-strip matching was calculated (Table 3-6).

As summarized in Table 3-6, compared to intra-strip matchings, there was a significant decrease (approximately four times) in the average ratio of adjacent inter-strip matchings when the pitch angle increased from 20° to 40°, regardless of the GSDs. This result demonstrates that, when image acquisition occurs at a 40° pitch angle, the number of matches among adjacent inter-strip images may not be sufficient for the SfM process. This resulted in an alignment failure rate of over 10% (as shown in the last column of Table 3-5) and a significantly large RMS error for all validation points in some cases, as reported for GSD20.

Close inspection of each main strip in the image-sets with a 40° pitch angle (Table 3-7) revealed that the last main strips had the lowest ratio of adjacent inter-strip to intra-strip matching. This can lead to alignment failure and significantly large RMS errors at all validation points.

Table 3-6. Average ratio of adjacent inter-strip matchings to intra-strip matchings for main-strips under a standard SfM setting observed in 20° and 40° pitch angles in three GSDs.

Image-set	GSD 10	GSD 15	GSD 20
Pitch angle 20°	68.81	76.97	68.35
Pitch angle 40°	14.83	21.50	17.09

Unit: % (percent)

Table 3-7. Percentage of adjacent inter-strip matching to **intra-strip matching in main-strips in single SfM setting for image-sets with 40° pitch angle.**

GSD	Main strips						
	ST1	ST3	ST5	ST7	ST9	ST11	ST13
GSD10_40	15.15	30.43	14.79	15.32	11.85	11.16	5.11
GSD15_40	19.66	37.40	25.63	17.76	7.04		
GSD20_40	15.97	29.43	16.18	6.77			

Unit: % (percent)

In summary, the robustness of the SfM accuracy and precision was evident over 750 analysis settings (with two trials per setting) using 15 image sets captured at five pitch angles and three distinct GSDs. In the discussion section, we explore the possible reasons for these findings and highlight their importance for UAV-based photogrammetry in both practice and research.

3.4. Discussion

Initially, we discuss pitch angles that exhibit robustness against non-optimal analysis settings, followed by an exploration of pitch angles that are not robust. Finally, potential directions for future research and limitations of this study were discussed.

3.4.1. Pitch angles robust against non-optimal analysis settings

This study's experiments on UAV-based photogrammetry utilizing a CPA-2D-GP flight design demonstrated the accuracy and precision of SfM against non-optimal analysis settings for certain pitch angles. Specifically, utilizing 15 image sets with three GSDs, it was shown that image-sets captured with 20° and 30° pitch angles resulted in small RMS errors of less than 0.056 m and 0.046 m, respectively, for all validation points over a variety of SfM settings (750). These levels of RMS error cannot be solely attributed to SfM because they are comparable to the RMS error observed in the RTK-GNSS measurements of shooting positions and validation points. Based on these findings, a CPA-2D-GP flight design with 20° and 30° pitch angles can be employed using the default settings.

Another contribution of this study is the investigation of the best pitch angles for a CPA-2D-GP flight design in SfM processing using particular analysis settings. Several studies have investigated the optimal pitch angles in hybrid flight designs of conventional parallel-viewing-direction shooting and supplemental tilted shooting [10,14,23,36,47]. Ahmed et al. [48] evaluated the performance of a

constant pitch using limited image sets captured at pitch angles of 20° , 0° , and a combination of both, but utilized only a single SfM analysis setting. Although Nesbit and Hugenholtz [23] examined the accuracy of a 3D model (generated from camera parameters estimated by SfM) by adopting a CPA-2D-GP flight design to acquire a wide range of image sets (from 0° to 35°), they did not mention validation point errors or camera estimation errors, which are essential for investigating the accuracy and precision of SfM. Importantly, the optimal pitch angles from 20° to 30° for CPA-2D-GP flight design, previously reported by Takata et al. (2021) [24] using ten image-sets captured at GSD 20 and two overlap ratios, was confirmed in this study by utilizing 15 image sets at three GSDs (10, 15, and 20).

3.4.2. Pitch angles not robust against non-optimal analysis settings

Many studies have highlighted the poor results and low consistency of images acquired using CPA-2D-GP flight design with a 0° pitch angle under default settings [10,15,36]. This study reaffirmed the well-documented limitations of using this pitch angle across 750 SfM analysis settings. Such challenges arise predominantly because image sets with viewing directions parallel to the ground surface make it impossible to estimate the most important intrinsic parameter, the focal length (f) [47]. Furthermore, camera position measurements by RTK-GNSS attached to P4RTK do not aid in the estimation of f because cameras are placed at the same altitude. This led to a large alignment failure ratio and a large interquartile range of RMS errors for all validation points.

This study demonstrates that shooting with pitch angles lower than 10° and at 40° can negatively affect SfM performance in many aspects, depending on the analysis settings. Specifically, poor SfM performance was observed in the CPA-2D-GP flight design using 10° pitch angles, resulting in a large RMS error for all validation points, with the vertical error being the primary component in several of the 750 SfM analysis settings. A strong negative correlation was also found between the mean vertical error of the validation points and the estimated intrinsic parameters, particularly the focal length f . Previous studies have documented similar issues with low pitch angles when using the default settings or other combinations of SfM analysis settings [10,20,36]. These results suggest that the most likely reason for systematic vertical errors when using low-pitch angles, such as 10° is the incorrect estimation of the intrinsic parameter f by SfM. Although the 10° pitch angle deviates from nadir viewing, it may still be insufficient for SfM to accurately estimate f , leading to an unstable estimation of f for images captured at this pitch angle.

Numerous studies on the SfM accuracy have discussed the risk of matching failures between images when there is a significant angle between the optical axes [41,47,49]. Moreels and Perona [49] reported that optical angles larger than 30° were problematic for popular feature detectors such as the Scale-Invariant Feature Transform (SIFT) used for automated image matching. Our study shows that a CPA-2D-GP flight design with a pitch angle of 40° may lead to alignment failure in

SfM processing, depending on the analysis settings. Although the acceptable angle depends on the target surface and texture, the inter-strip matching in this study failed in certain analysis settings when the pitch angle was set to 40° . In such cases, the optical axes of the two images in adjacent strips have an angle of 80° , causing the surface points to appear in more distinct ways and making inter-strip matching more difficult. When images in a strip lack matching with images in adjacent strips, they simply compose an isolated block of parallel-viewing images for which the estimation of focal length is impossible, such as images taken at a pitch angle of 0° . This results in a risk of alignment failure for some analysis settings of images captured at a pitch angle of 40° .

3.4.3. Limitations and future research

While this study focused on evaluating the robustness of SfM accuracy and precision in relatively flat and unvegetated terrain, further research is required to examine whether these findings are generalizable in more complex environments. Additional discussion is provided in Chapter 6.

Liu et al. [50] introduced an innovative method that integrates flight configuration factors such as flight height, average image quality, image overlap, ground control point quantity, and camera focal length to predict the accuracy of UAV-SfM photogrammetry. These methods can significantly aid in refining survey planning. However, to validate the reliability of this method, a comprehensive assessment across various SfM - analysis settings, instead of a single setting, is essential.

3.5. Conclusion

In this study, the robustness of SfM in UAV-based photogrammetry against non-optimal analysis settings was evaluated using a popular flight design, CPA-2D-GP, for a relatively flat surface. The SfM accuracy and precision were evaluated for 750 different analysis settings for each of the 15 UAV image sets (taken at five pitch angles and three distinct ground sample distances, with two trials per setting). The results demonstrated that pitch angles of 20° and 30° are the most robust against non-optimality in the SfM settings, given the small RMS errors for all validation points (no larger than 0.056 m). This helps alleviate concerns regarding the SfM settings when using these pitch angles, as opposed to others.

By contrast, flights with 40° pitch angle exhibited a higher risk of pose estimation failure, depending on the SfM settings. Using this pitch angle requires running the SfM in various settings and selecting the one with the most successful pose estimation. Additionally, shooting with 10° pitch angles may be insufficient for accurately estimating the intrinsic parameters (particularly the focal length f), depending on the analysis settings.

In the evolving domain of UAV-based photogrammetry, the robustness of SfM accuracy and precision across various analysis settings is vital. The outcomes of this study contribute to a deeper understanding of SfM behaviors and lay a foundation for future investigations. As the discipline

advances, insights from this study will serve as a guide for practitioners and researchers, leading them toward enhanced reliability and consistency in SfM applications.

Chapter 4. Indeterminacy of camera intrinsic parameters in Structure from Motion using images from Constant-Pitch Angle flight design

4.1. Introduction

Intrinsic parameter estimation by self-calibration is commonly used in UAV-based photogrammetry with SfM. However, obtaining stable estimates of these parameters from image-based SfM - which relies solely on images, without auxiliary data such as ground control points (GCPs) - remains challenging. Aerial imagery acquired with the Constant-Pitch-Angle, One-Directional, and Gridded-Position flight design (CPA-1D-GP) (Fig 2.7b) often exhibits non-linear deformations, highly unstable intrinsic parameters, and even alignment failures flights [32]. It is hypothesized that the CPA-1D-GP flight design forms a “critical configuration” - certain combinations of camera motion and scene geometry - can introduce indeterminacy into the bundle adjustment with self-calibration [33].

In this study, the indeterminacy of two basic intrinsic parameters f and cy , which showed significant instabilities in the previous experiments [32], was investigated through numerical simulations. These numerical findings were validated using real datasets acquired at three different ground sampling distances (GSDs). Finally, a practical mitigation strategy was explored to stabilize intrinsic parameter estimation in image-based SfM. By bridging the theoretical - practical gap, this study aims to contribute to more reliable UAV-SfM workflow that does not depend on auxiliary information.

4.2. Methods

4.2.1. Fundamental of self-calibration in SfM

Suppose P is a 3D ground point that is visible in multiple images captured from different viewpoints (cameras A, B, C), as shown in Fig 4-1. The geometric relationship between the 3D point and its 2D projections on each image is described by collinearity equations as follows:

$$\begin{cases} x = -f \frac{\alpha_{11}(X-X_0) + \alpha_{21}(Y-Y_0) + \alpha_{31}(Z-Z_0)}{\alpha_{13}(X-X_0) + \alpha_{23}(Y-Y_0) + \alpha_{33}(Z-Z_0)} \\ y - cy = -f \frac{\alpha_{12}(X-X_0) + \alpha_{22}(Y-Y_0) + \alpha_{32}(Z-Z_0)}{\alpha_{13}(X-X_0) + \alpha_{23}(Y-Y_0) + \alpha_{33}(Z-Z_0)} \end{cases} \quad (4-1)$$

where:

- (x, y) : image coordinates of the projection of ground point.
- (X, Y, Z) : object space coordinates of the ground point.
- (X_0, Y_0, Z_0) : object space coordinates of the camera projection center.
- cy : y-coordinate of the principal point in the image.
- f : camera focal length.

- $\alpha_{1i}, \alpha_{2i}, \alpha_{3i}$ ($i = 1, 2, 3$): elements of the rotation matrix formed by three rotation angles.

The collinearity equations contain three categories of unknowns:

- Extrinsic parameters: parameters representing relative position and the orientation of each camera.
- Intrinsic parameters: parameters representing the geometric characteristics of the camera, such as focal length and principal points. Note that only two parameters f and cy are considered in this study and in Equation (4-1).
- Three-dimensional point coordinates: relative coordinates of scene points in object space.

These parameters are estimated simultaneously in the bundle adjustment (BA) of SfM by minimizing the overall reprojection error. The reprojection error of point i onto image j can be expressed as follows:

$$\begin{cases} F_{ij} := x_d - x_p = x_d + f \frac{\alpha_{11}(X-X_0) + \alpha_{21}(Y-Y_0) + \alpha_{31}(Z-Z_0)}{\alpha_{13}(X-X_0) + \alpha_{23}(Y-Y_0) + \alpha_{33}(Z-Z_0)} \\ G_{ij} := y_d - y_p = y_d + cy + f \frac{\alpha_{12}(X-X_0) + \alpha_{22}(Y-Y_0) + \alpha_{32}(Z-Z_0)}{\alpha_{13}(X-X_0) + \alpha_{23}(Y-Y_0) + \alpha_{33}(Z-Z_0)} \end{cases} \quad (4-2)$$

where (x_p, y_p) are the 2D projected coordinates computed via the collinearity equations and (x_d, y_d) are the 2D observed image coordinates of the point.

In SfM, for successful camera estimation, the objective function - root mean square (RMS) reprojection error - must have a unique global minimum. If multiple minima exist, the optimization becomes ambiguous, and SfM fails to produce reliable camera parameters. Parameters with multiple minimizing values are considered indeterminate. In such cases, a specific combination of camera motion and scene geometry that generates images impossible to unique estimation of certain intrinsic parameters is referred to as critical configuration (Fig 4-1).

4.2.2. Numerical experiments

The indeterminacy of f and cy was investigated by analyzing RMS reprojection error, which is the objective function to be minimized at the BA stage in SfM. This was achieved by fixing either f or cy to incorrect values in BA and estimating the other parameters along with extrinsic parameters and tie points. If RMS reprojection error remains nearly unchanged regardless of the input values of f or cy , it indicates that these parameters do not influence the objective function, thereby demonstrating their indeterminacy in SfM.

a) Synthetic image acquisition

This study used Blender version 2.79b [51], an open-source computer graphic (CG) software program, to generate a flat plane with the dimensions of 400 m \times 400 m and randomly place multiple rectangular parallelepiped objects of various sizes on it. Various random textures with a resolution of 5940 \times 8410 pixels were applied to the plane and objects. These textures included local features suitable for matching in SfM, as shown in Fig 4-2.

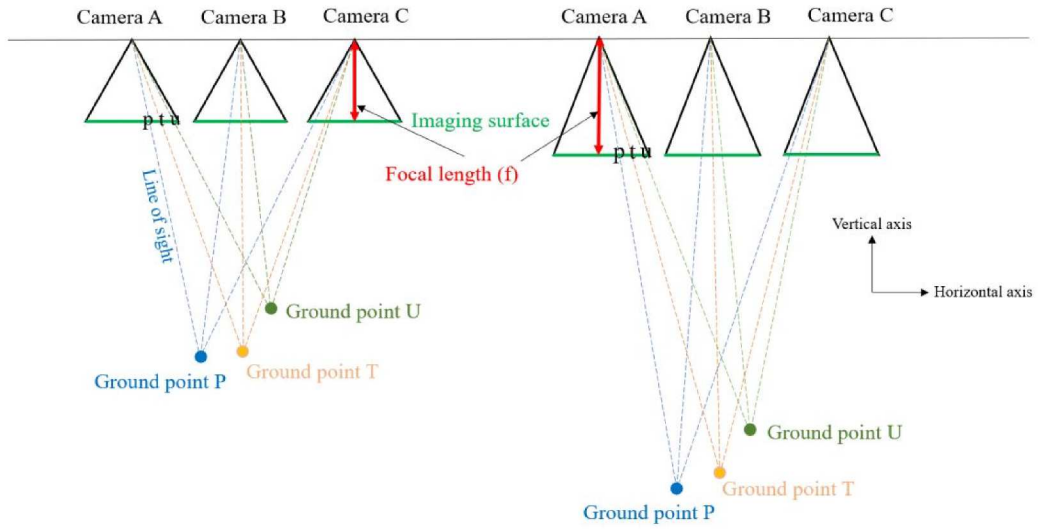


Figure 4-1. Example of a critical configuration where the focal length f cannot be determined from parallel shooting images.

In this situation, multiple values of f can be estimated, making it impossible to uniquely determine the correct value.

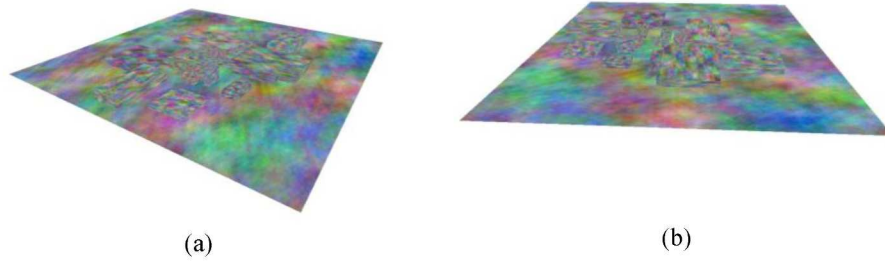


Figure 4-2. Two views of the target used for image acquisition in the numerical experiments: (a) Side view; (b) Front view

The synthetic image acquisition of the target was performed using the image and camera specifications described in Table 4-1. In CG space, six image-sets were generated using six different flight designs, divided into two groups as Table 4-2.

Table 4-1. Camera specifications used in CG space

Parameters	Value
Pin hole camera	Linear camera with no distortion
Focal length (pixels)	1824
Image size (pixels)	2736×1824

Table 4-2. Classification of flight designs in numerical experiments

Flight designs without an intermediate strip	Flight designs with an intermediate strip
1. Constant-Pitch-Angle, One-Directional and Gridded-Position (CPA-1D-GP) flight design	1. CPA-1D-GP flight design with one additional image on a single intermediate strip
2. Constant-Pitch-Angle, One-Directional and Random-Position (CPA-1D-RP) flight design	2. CPA-1D-GP flight design with one additional image on each of the three intermediate strips
	3. Constant-Pitch-Angle, Two-Directional, and Gridded-Position (CPA-2D-GP) flight design.
	4. CPA-1D-RP flight design with one additional image in a single intermediate strip

The intermediate strip refers to a short flight path positioned between two primary strips, illustrated as green-blue arrows in Table 4-3. The pitch angle was set to 20° for all six flight designs, and the flight altitude was fixed at 73 m to achieve a GSD of 40 mm. The details of flight designs are provided in Table 4-3. In this study, a 20° pitch angle was selected based on its proven effectiveness in enhancing UAV-SfM calibration from previous studies [19,23,48,52,53] and its confirmed robustness in SfM accuracy and precision across various analysis settings [20,32]. The indeterminacy of f and c_y was examined with this best performing pitch angle, which serves as a representative case for indeterminacy under other pitch angles.

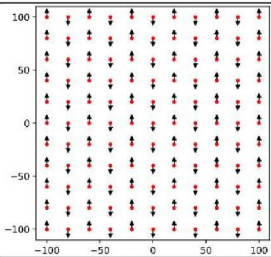
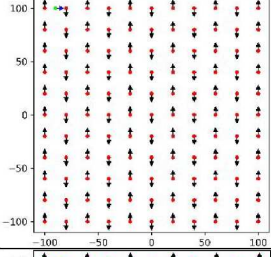
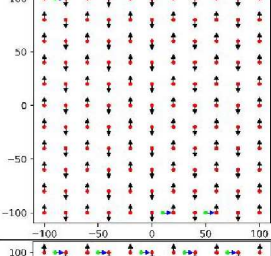
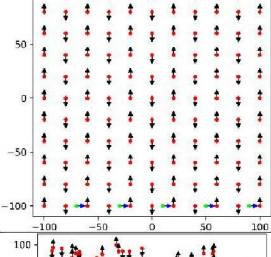
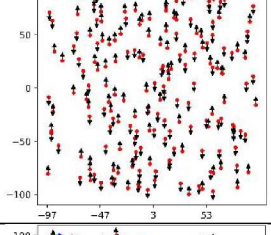
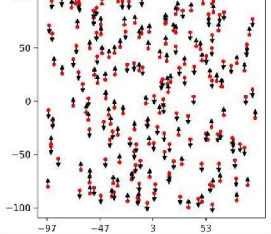
b) SfM processing

For each simulated image-set created in CG space, SfM was performed using the commercial software Agisoft Metashape version 1.5.5. The SfM workflow (Fig 4-3) began with “align photos”, followed by bundle adjustment (BA) with the camera parameters effectively fixed to their true values to generate an accurate set of tie points. The settings used are detailed in Table 4-4.

Based on these tie points, a camera intrinsic parameter (either f or c_y) was fixed to values higher than true value (v_+) and values lower than true values (v_-), while the other parameter (c_y or f) was not fixed. Then, BA was rerun. In this process, BA was performed using the previously generated accurate tie points. This approach enabled observation of RMS reprojection error behaviour in relation to the fixed intrinsic parameters (f or c_y).

Table 4-3. Descriptions of six image-sets taken by six flight designs in numerical experiments.

Flight Design	Description	Strip Interval/Images Interval in One Strip (Meters)/Number of Images	Illustration
----------------------	--------------------	--	---------------------

Constant-Pitch-Angle, One-Directional and Gridded-Position flight design (CPA-1D-GP)	The camera is tilted at a fixed pitch angle along the flight lines, and when drones fly in the opposing direction, the local convergence is achieved.	20/20/121	
CPA-1D-GP flight design with one additional image on a single intermediate strip.	Only one image with the same pitch angle was added at the midpoint of a single intermediate strip (strip between two flight lines) in the CPA-1D-GP flight design.	20/20/122	
CPA-1D-GP flight design with one additional image on each of the three intermediate strips	Three images with the same pitch angle were added at the midpoint of three randomly selected intermediate strips in the CPA-1D-GP flight design.	20/20/124	
Constant-Pitch-Angle, Two-Directional, and Gridded-Position flight design (CPA-2D-GP)	One image with the same pitch angle was added at the midpoint of each intermediate strip in the CPA-1D-GP flight design	20/20/131	
Constant-Pitch-Angle, One-Directional and Random-Position flight design (CPA-1D-RP)	Cameras were randomly placed on the horizontal plane at 73 m above the target plane. Each camera was oriented in one of the two orientations appearing in the CPA-1D-GP flight design.	Random/random /200	
CPA-1D-RP flight design with one additional image in a single intermediate strip	Only one image with the same pitch angle was added to the intermediate strip in the CPA-1D-RP flight design.	Random/random /201	

Black-red arrows indicate image positions along the main flight strips, while green-blue arrows indicate those in the intermediate strips. The arrow size corresponds to the camera pitch angle. In this study, all CP flight designs used a fixed pitch angle of 20 degrees.

Table 4-4. Settings for “Alignment” used to generate accurate tie points.

Parameters	Values
Input image size	High (original size) (2736 x 1824 pixels)
Key point limit	50,000
Intrinsic parameters estimation	Fixed to true value during BA.

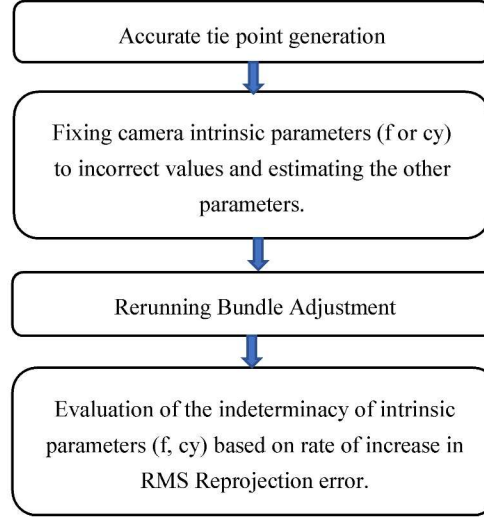


Figure 4-3. SfM flow in numerical experiments to evaluate the indeterminacy of each intrinsic parameter (f or cy).

c) Evaluation of the indeterminacy of camera intrinsic parameters in SfM

To evaluate the indeterminacy of camera intrinsic parameters in SfM, the variation in RMS reprojection error was analyzed between two BA conditions: (1) BA with the intrinsic parameters (f and cy) fixed to their true values and (2) BA with f or cy fixed to incorrect values. The degree of variation was quantified by the rate of increase in RMS reprojection error, which serves as an indicator of how inaccurate intrinsic parameters influence the SfM and helps identify occurrences of their indeterminacy. In principle, the objective function minimized during BA - RMS reprojection error - must have a unique global minimum. The presence of multiple local minima, dependent on different fixed intrinsic parameter values, indicates that the SfM process is unable to uniquely determine these parameters. In such cases, the corresponding intrinsic parameters are considered as indeterminate.

Additionally, fixing either f or cy to incorrect values while estimating the remaining parameter (cy or f, respectively) provides insight into the correlation between f and cy.

The rate of increase in RMS reprojection error is calculated as follows:

$$R_{increase} = \frac{E_{incorrect} - E_{true}}{E_{true}} \quad (4-3)$$

Where: R_{increase} is the rate of increase in RMS reprojection error.

$E_{\text{incorrect}}$ (pixels) is RMS reprojection error when fixing either f or c_y to the incorrect values and estimating the remaining parameter in BA.

E_{true} (pixels) is RMS reprojection error when fixing both f and c_y to true values (1824 and 0 pixels, respectively) in BA.

4.2.3. Real-data analysis

a) Study site

The in-situ data in this study partially utilized the data from chapter 3. These images captured an area of around 100 x 100 m², located in Tsukubamirai city, Ibaraki prefecture, Japan. This area was constructed for housing purposes. Fig 4-4 shows the ground condition of the target terrain, mostly bare land covered with short vegetation.

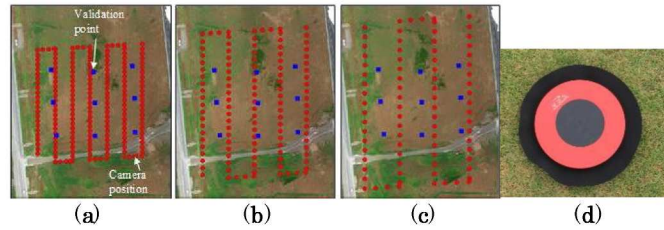


Figure 4-4. Camera positions and validation points at the study site overlaid with orthophotos generated by GSD10 (a), GSD15 (b), GSD20 (c) using CPA-2D-GP flight design. At each validation point, world coordinates were measured by Aero markers (d) with a built-in GNSS receiver.

b) Image acquisition

Aerial photos were collected using DJI Phantom 4 RTK [54]. This UAV can measure the camera position at the time of exposure by RTK-GNSS (real-time kinematic global navigation satellite system) positioning. A set of nine validation points (Fig 4-4) was employed to evaluate the accuracy of the SfM performance using the Aero marker [44]. The Aero markers used for ground validation were manufactured by Aero, Inc., Tokyo, Japan. Each Aero marker is equipped with an integrated GNSS receiver, enabling it to record the coordinates at the center of a 24 cm diameter circular target with sub-centimeter accuracy. The red-and-black reflective pattern of the marker is designed to enhance automatic detection by SfM processing software, such as Agisoft Metashape version 1.5.5, which was used in this study.

A flight design similar to CPA-2D-GP was adopted for data acquisition. This flight pattern was generated using the 3D photogrammetry preset feature in the P4RTK system to capture images at two-second intervals and record camera coordinates via RTK-GNSS during image capture. In these CPA-2D-GP flights, the camera was tilted at a fixed pitch angle of 20° along the flight lines, and the consecutive images with yaw angle deviation over 10° from the main flight line, taken during the

drone rotation, were referred to as the intermediate strips. They were removed to simulate three image sets of CPA-1D-GP flight design (Fig 4-5).

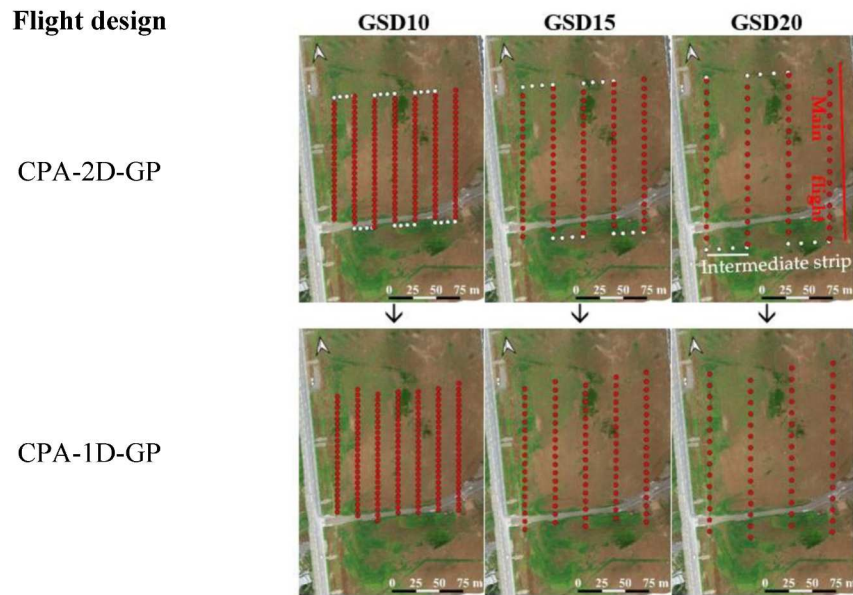


Figure 4-5. Generation of CPA-1D-GP flight design from CPA-2D-GP flight design used in real-data analysis

Red dots indicate image positions in the main flight strips, while white dots represent image positions in the intermediate strips.

In this study, P4RTK was flown at three altitudes of 73, 55, and 36 m above ground level (at the drone's home point), which yielded three GSDs of 20, 15, and 10 mm, respectively. All photographs were captured along parallel flight lines with an overlap ratio of 80% forward and 60% side lap when the camera's optical axis was oriented toward nadir. The details of the image-sets used in the real-data analysis are described in Table 4-5.

Table 4-5. Summary of three CPA-2D-GP flights acquired by P4RTK and three CPA-1D-GP flights in real-data analysis.

Shooting Attitude [m]	Flight design		Overlap Ratio [%]
	CPA-2D-GP	CPA-1D-GP	
73 (GSD20)	74	61	80% forward, 60% side lap.
55 (GSD15)	107	91	
36 (GSD10)	187	163	

c) SfM Processing

For each image set, SfM was performed following the “align photos” in Agisoft Metashape version 1.5.5 software. In this process, camera parameters were estimated by using images only, then the point clouds were georeferenced using projection centers recorded by RTK-GNSS embedded in the images taken by P4RTK. The absolute coordinates of the validation points evaluated by multi-view triangulation using camera parameters estimated in SfM were used to validate the accuracy of the SfM-derived model, in accordance with the nine validation points. It is worth to note that in this study self-calibration was performed using images only, without additional information.

SfM was tested through a combination of SfM analysis settings summarized in Table 4-6, resulting in 30 settings with 50 trials for each image-set listed in Table 4-5. This analysis was conducted to observe the variation in the estimation of intrinsic parameters under different SfM settings.

Table 4-6. Summary of the analysis settings tested in this study.

Setting items	Meaning	Setting values
Align photos Accuracy	Set the size of input images (shrinkage ratio) for feature extraction. • High: used original size. • Medium: image downscaled by a factor of two at each image side.	High, medium
Key point limit	Set the maximum number of feature points detected in each image.	1/2, 1/3, 1/4 of the average number of detectable keypoints for the input images, corresponding to: ✓ 35643, 23762, 17821 when the size of input images is set as High. ✓ 8229, 5486, 4115 when the size of input images is set as Medium.
Tie point limit	Set the maximum number of tie points to be detected in each image.	0 It will attempt to detect as many tie points as possible in each image.
Optimize camera alignment	Set the intrinsic parameters considered in Brown models.	① f, cx, cy, k1-k4, p1-p4, b1, b2 ② f, cx, cy, k1-k4, p1-p4 ③ f, cx, cy, k1-k4, p1-p2 ④ f, cx, cy, k1-k3, p1-p4 ⑤ f, cx, cy, k1-k3, p1-p2
2 x 3 x 5 = 30 analysis settings with 50 trials/setting, equivalent to 1500 trials for each image set.		

In order to evaluate the variation of intrinsic parameters estimates in one SfM setting, a standard SfM setting was repeated in 50 times (trials), with the following parameters:

- Size of input images for feature detection: High
- Keypoint limit: a half ($\frac{1}{2}$) to the average number of detectable keypoints for the input images (35643).
- Intrinsic parameters considered in Brown models: f, cx, cy, k1-k3, p1-p2.

d) Intrinsic parameters estimation and error evaluation

In this study, the variation of intrinsic parameter estimation (f and cy) was quantified, in accordance with the accuracy and precision of SfM for each image-set. The accuracy and precision

of SfM were evaluated using the RMS error of all nine validation points for each analysis setting, as recommended by James et al. [55].

Additionally, statistical analyses were conducted on the total RMS error (Val_RMSE_T) and the vertical RMS error (Val_RMSE_Z) computed from all validation points for both a standard setting (with 50 trials) and 30 settings such as the maximum value, 75th percentile (Q3), 50th percentile (Q2), and interquartile range (IQR). For each of the 30 settings, the mean values of the estimated f , cy , Val_RMSE_T, and Val_RMSE_Z of all the validation points were first calculated over 50 repeated trials. These mean values were subsequently used to derive the statistical indicators (maximum, Q3, Q2, and IQR), thereby enabling a comparative assessment of SfM accuracy and precision across different settings.

Moreover, the mean vertical error of all nine validation points (MEZ) was evaluated for each analysis setting. The mean vertical error is defined as the average difference between the estimated elevation of the validation points (derived using camera parameters estimated by SfM) and the measured elevation of corresponding validation points obtained by Aerobo markers.

4.3. Results

The results are divided into two main sections: numerical experiments and real-data analysis. In the numerical experiments, we present the verification of the indeterminacy of intrinsic parameters in image-based SfM for six flight designs. The real data analysis focuses on three points: the estimates of camera intrinsic parameters (f , cy) across multiple repetitions of a single SfM setting and in various SfM settings, and the correlation between the estimates of f and the mean vertical error (MEZ) for all validation points.

4.3.1. Numerical experiments

This section verifies the indeterminacy of intrinsic parameters in image-based SfM by analyzing six different flight designs. The RMS reprojection error and its rate of increase were analyzed to evaluate the sensitivity of SfM when the intrinsic parameters were fixed to inaccurate values relative to their true values (Fig 4-6 and 4-7).

As shown in Fig 4-7, the rate of increase in RMS reprojection error was zero for images captured by flight designs without image in the intermediate strip including the CPA-1D-GP and CPA-1D-RP flight design. In contrast, for flight designs with images in the intermediate trip, including the CPA-1D-GP flight design with one additional image on a single intermediate strip, CPA-1D-GP flight design with one additional image on each of the three intermediate strips, CPA-2D-GP, and CPA-1D-RP flight design with one additional image in a single intermediate strip, the rate of increase in RMS reprojection error ranged from 1.1 to 7.6.

Fixed value setting (pixels)			CPA-1D-GP		CPA-1D-GP flight design with one additional image on a single intermediate strip		CPA-1D-GP flight design with one additional image on each of the three intermediate strips		CPA-2D-GP		CPA-1D-RP		CPA-1D-RP flight design with one additional image in a single intermediate strip	
			$E_{\text{incorrect}}$ (pixels)	Estimated cy (pixels)	$E_{\text{incorrect}}$ (pixels)	Estimated cy (pixels)	$E_{\text{incorrect}}$ (pixels)	Estimated cy (pixels)	$E_{\text{incorrect}}$ (pixels)	Estimated cy (pixels)	$E_{\text{incorrect}}$ (pixels)	Estimated cy (pixels)	$E_{\text{incorrect}}$ (pixels)	Estimated cy (pixels)
f	v ₋	1641.6	0.058	141.20	0.213	135.81	0.334	126.91	0.470	111.38	0.060	141.20	0.168	137.81
	v ₊	2006.4	0.058	186.12	0.250	186.29	0.380	186.35	0.505	186.86	0.060	186.12	0.197	186.63
cy	v ₋	-100	0.058	1,936.95	0.162	1,939.06	0.262	1,944.43	0.398	1,956.52	0.060	1,936.95	0.130	1,938.35
	v ₊	100	0.058	1,697.72	0.160	1,695.96	0.258	1,691.68	0.398	1,680.83	0.060	1,697.72	0.129	1,696.56
			E_{true} (pixels)		E_{true} (pixels)		E_{true} (pixels)		E_{true} (pixels)		E_{true} (pixels)		E_{true} (pixels)	
f	True value	1824	0.058		0.058		0.058		0.059		0.060		0.060	
cy	True value	0												

Figure 4-6. RMS reprojection error and estimated parameter values when fixing parameter f or cy to incorrect values for six flight designs.

$E_{\text{incorrect}}$: RMS reprojection error when fixing either f or cy to the incorrect values and estimating the remaining parameter in BA. E_{true} : RMS reprojection error when fixing both f and cy to true values (1824 and 0 pixels, respectively) in BA. Red and blue indicate the estimated intrinsic parameters (f and cy), while green represents the RMS reprojection error (in pixels). The bar length is scaled relative to the maximum value within each group.

Fixed value setting (pixels)			Rate of increase in RMS reprojection error (R_{increase})					
			CPA-1D-GP	CPA-1D-GP flight design with one additional image on a single intermediate strip	CPA-1D-GP flight design with one additional image on each of the three intermediate strips	CPA-2D-GP	CPA-1D-RP	CPA-1D-RP flight design with one additional image in a single intermediate strip
f	v ₋	1641.6	0.0	2.7	4.7	7.0	0.0	1.8
	v ₊	2006.4	0.0	3.3	5.5	7.6	0.0	2.3
cy	v ₋	-100	0.0	1.8	3.5	5.8	0.0	1.2
	v ₊	100	0.0	1.8	3.4	5.8	0.0	1.1

Figure 4-7. Rate of increase in rms reprojection error when fixing parameter f or cy to incorrect values for six flight designs.

Green represents the rate of increase in RMS reprojection error (R_{increase}). The bar length is scaled relative to the maximum value in the table.

In CPA-1D-GP and CPA-1D-RP flight design, the RMS reprojection error remained unchanged regardless of whether the intrinsic parameters f or cy was fixed to true or incorrect values in BA. However, in flight designs with images in the intermediate strip, the addition of one image between two flight lines resulted in a noticeable increase in RMS reprojection error. Moreover, when f was fixed to incorrect values, the estimates of cy derived from BA were strongly inaccurate compared to the true value (0), and vice versa (Fig 4-6).

These results demonstrate that both f and cy are indeterminate in image-based SfM. In CPA-1D-RP flight design, where camera positions were randomly distributed compared to CPA-1D-GP flight design, and the camera orientation remained fixed at 20° forward and backward, the RMS reprojection error remained unchanged regardless of whether the intrinsic parameters were fixed to incorrect or true values. This indicates that altering the shooting positions alone does not resolve the indeterminacy.

In contrast, for flight patterns with at least one image in the intermediate trip, the values of f or cy had a substantial impact on RMS reprojection error, with rates of increase in RMS reprojection error exceeding 7.6 for f and 5.8 for cy (Fig 4-7). This demonstrates that f and cy become determinable in image-based SfM when at least one image is added to the intermediate strip.

In summary, the numerical experiments showed that the intrinsic parameters f and c_y are indeterminate in image-based SfM when using aerial images captured by flight designs without an intermediate strip such as the CPA-1D-GP flight design. Adding images of the intermediate strips effectively resolve the indeterminacy of f and c_y .

In the next section, we will evaluate the estimation of intrinsic parameters in image-based SfM using in situ data captured by CPA-1D-GP and CPA-2D-GP flight design.

4.3.2. Real-data analysis

a) Estimates of camera intrinsic parameters (f , c_y) across 50 trials of a single SfM setting

Fig 4-8 presents the results of a standard SfM setting for six image-sets captured at three different GSDs using two flight designs: the CPA-1D-GP and CPA-2D-GP. Across 50 repeated trials of a standard SfM setting, the standard deviation in the estimates of intrinsic parameters f and c_y was zero for the image-sets taken by the CPA-2D-GP flight design, indicating a highly stable estimation. In contrast, image-sets from the CPA-1D-GP flight design showed substantial variability with a standard deviation of 0.32 pixels for f and 0.08 pixels for c_y . This instability also resulted in a 0.008 m and 0.009 m deviation in the interquartile range (IQR) of total RMS error (Val_RMSE_T) and vertical RMS error (Val_RMSE_Z), respectively.

These results demonstrate that the estimation of f and c_y is unstable in image-based SfM when using images from the CPA-1D-GP flight. However, in the CPA-2D-GP flight design, where additional images are captured in the intermediate strips of the CPA-1D-GP flight design, the estimation of these parameters becomes more stable, even within a single SfM setting.

	Image-sets	Standard deviation		50 percentile				75 percentile				Maximum				IQR			
		f [pix]	of cy [pix]	Val	RMSE	Z	Val	RMSE	Z	Val	RMSE	Z	Val	RMSE	Z	Val	RMSE	Z	
GSD20	CPA-1D-GP	0.29	0.08	0.14	0.17	0.14	0.17	0.17	0.19	0.009	0.008								
	CPA-2D-GP	0.00	0.00	0.12	0.13	0.12	0.13	0.12	0.13	0.000	0.000								
GSD15	CPA-1D-GP	0.32	0.07	0.08	0.12	0.09	0.12	0.10	0.13	0.007	0.007								
	CPA-2D-GP	0.00	0.00	0.09	0.10	0.09	0.10	0.09	0.10	0.000	0.000								
GSD10	CPA-1D-GP	0.20	0.07	0.08	0.12	0.08	0.13	0.08	0.13	0.004	0.006								
	CPA-2D-GP	0.07	0.05	0.05	0.07	0.06	0.07	0.06	0.08	0.002	0.003								

Figure 4-8. Intrinsic parameter estimation and statistics of total RMS error (Val_RMSE_T) and vertical RMS error (Val_RMSE_Z) of all validation points for each image-set (one SfM analysis setting with 50 trials).

Dark blue represents the standard deviation of the estimated intrinsic parameters (f and c_y) in pixels, calculated from 50 trials of one SfM analysis settings. Green and bright blue represent Val_RMSE_Z and Val_RMSE_T, respectively, at the 50th, 75th, and maximum values, calculated from 50 trials of one SfM analysis settings. Orange indicates the interquartile range (IQR) of Val_RMSE_Z and Val_RMSE_T. In all cases, the bar length is scaled relative to the maximum value within each group.

b) Estimates of camera intrinsic parameters (f and c_y) across 30 SfM settings.

The estimates of f and c_y in image-based SfM obtained from 30 different SfM settings, each repeated 50 times, exhibited instability (Fig 4-9). The standard deviation of f ranged from over 1 pixel to 7.3 pixels, while the standard deviation of c_y ranged from 0.6 to 3.1 pixels. This instability

was particularly pronounced when using images from the CPA-1D-GP flight design, where the standard deviation was about six times higher for f and five times higher for cy (GSD20 image-sets) compared to those taken by the CPA-2D-GP flight design.

Image-sets		Standard deviation of f [pix]	Standard deviation of cy [pix]	50 percentile			75 percentile			Maximum			IQR		
				Val	RMSE	Z	Val	RMSE	T	Val	RMSE	Z	Val	RMSE	T
GSD20	CPA-1D-GP	7.290	3.108	0.078	0.089	0.167	0.186	0.739	0.757	0.132	0.131				
	CPA-2D-GP	1.252	0.627	0.050	0.059	0.102	0.109	0.138	0.144	0.078	0.058				
GSD15	CPA-1D-GP	6.244	2.383	0.139	0.151	0.183	0.205	0.426	0.453	0.110	0.105				
	CPA-2D-GP	1.267	0.689	0.027	0.039	0.066	0.076	0.102	0.117	0.054	0.047				
GSD10	CPA-1D-GP	3.708	2.357	0.055	0.085	0.099	0.157	0.275	0.330	0.069	0.102				
	CPA-2D-GP	1.022	0.860	0.026	0.046	0.043	0.066	0.055	0.073	0.029	0.031				

Figure 4-9. Intrinsic parameter estimation and statistics of total RMS error (Val_RMSE_T) and vertical RMS Error (Val_RMSE_Z) of all validation points for each image-set (30 analysis settings).

Dark blue represents the standard deviation of the estimated intrinsic parameters (f and cy) in pixels, calculated from 30 SfM analysis settings. Green and bright blue represent Val_RMSE_Z and Val_RMSE_T, respectively, at the 50th, 75th, and maximum values, calculated from 30 SfM analysis settings. Orange indicates the interquartile range (IQR) of Val_RMSE_Z and Val_RMSE_T. In all cases, the bar length is scaled relative to the maximum value within each group.

As shown in Fig 4-9, the RMS error of all the validation points was substantially higher for image-sets from the CPA-1D-GP flight design compared to those from the CPA-2D-GP flight design. For instance, in GSD15 image-set, the median RMS error of all the validation points (Val_RMSE_T) was 0.151 m, nearly four times greater than the 0.039 m observed for the CPA-2D-GP flight design. Similarly, the median vertical RMS error (Val_RMSE_Z) was approximately five times larger for the CPA-1D-GP flight design (0.139 m) compared to that for the CPA-2D-GP flight design (0.027 m). Furthermore, the accuracy and precision of SfM varied considerably across the 30 SfM settings for the CPA-1D-GP flight design image-sets. The interquartile range (IQR) of the RMS error of all validation points was 0.105 m for CPA-1D-GP flight designs, compared to 0.047 m for CPA-2D-GP flight designs (GSD15). Similar patterns were observed for image-sets from GSD10 and GSD20.

Overall, the estimates of f and cy were significantly less stable for images captured by CPA-1D-GP flight design than CPA-2D-GP flight design, both across multiple trials of a single setting and across different settings.

c) Correlation between the estimates of f and the mean vertical error for all validation points.

Theoretically, incorrect estimates of f lead to mean vertical error (MEZ) for all validation points in model reconstruction. As illustrated in Fig 4-10, a negative correlation was observed between the estimates of f and MEZ across 30 different SfM settings. This relationship can be explained by a simple pin hole camera model: as the estimated f increases, the triangulated ground point moves farther from the camera, causing its estimated vertical coordinate to decrease.

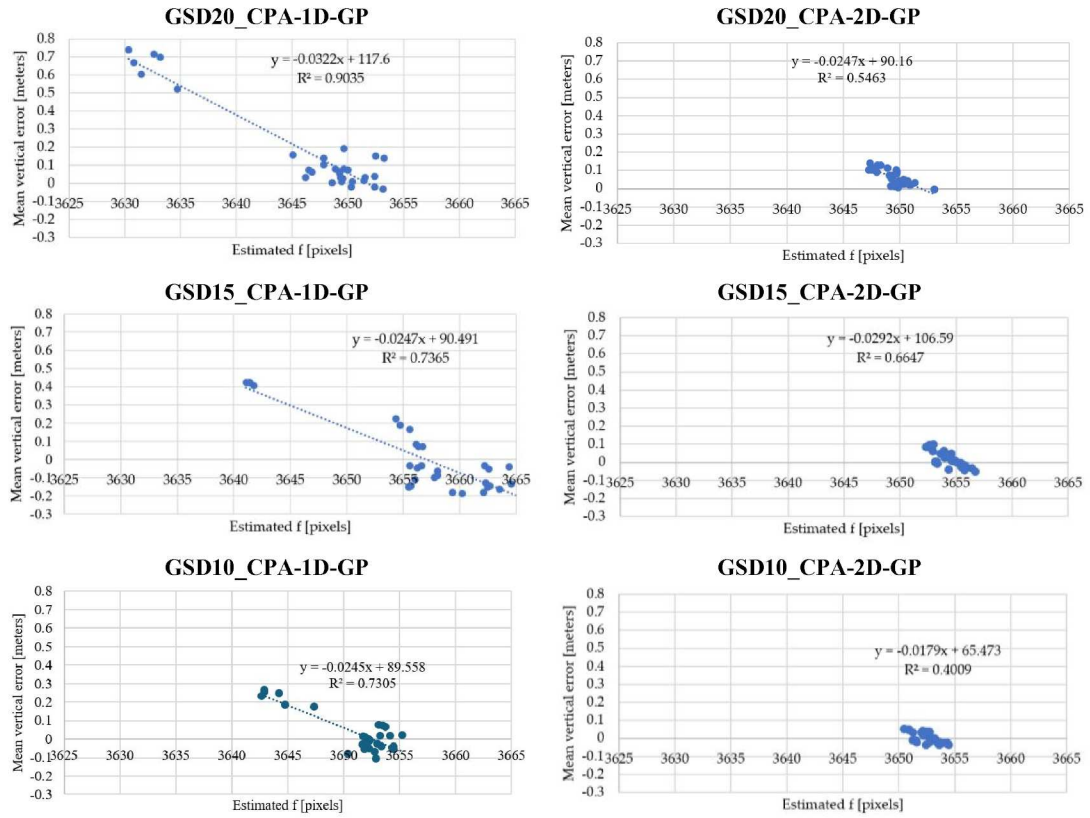


Figure 4-10. The correlation between estimated f and mean vertical error (MEZ)

To assess the contribution of vertical error due to incorrect f estimation to the total vertical error, the vertical error ratio was calculated as the proportion of the absolute mean vertical error (MEZ) to the total vertical error of all validation points (Val_RMSE_Z). As shown in Table 4-7, the average vertical error ratio for each image-set exceeded 80%, indicating that vertical error resulting from incorrect f estimation served as the primary contributor to the total vertical error, regardless of flight design.

Table 4-7. Average of vertical error ratio for each image-set (30 SfM analysis settings)

Image Sets	Average of Vertical Error Ratio (%)	
	CPA-1D-GP flight design	CPA-1D-GP flight design
GSD10	80.65	84.09
GSD15	80.71	97.84
GSD20	88.60	88.37

In summary, the indeterminacy of intrinsic parameters, especially f and cy, in image-based SfM has been demonstrated using six flight designs in numerical experiments, and its effect has been demonstrated in a real-data analysis using six image-sets. In the next section, we will discuss the implications of these findings on existing studies and suggestions for practical application.

4.4. Discussion

4.4.1. Indeterminacy of camera intrinsic parameters in images-based SfM

This study presents the first combined numerical and in-situ analysis of the indeterminacy of intrinsic parameters in images-based SfM for CPA-1D-GP flight design. The numerical experiments demonstrate that, when images are captured under a CPA-1D-GP flight design, f and c_y , are indeterminable in images-based SfM.

Critical configurations - specific combinations of camera motion and scene geometry- are known to induce intrinsic-parameter indeterminacy. Previous studies have extensively documented critical configurations related to linear images (images captured by pin hole camera without lens distortion) [33,56]. For example, planar motion over general terrain, in which camera moves on plane while rotating around an axis normal to that plane, prevents estimation of a single intrinsic parameter [33].

CPA-1D-GP flight represents a restrictive form of planar motion in which the camera's movement is constrained into a plane, and rotation is limited to only two orientations (pitch and yaw) rather than allowing free rotation around the roll axis. Therefore, it is possible that these additional constraints cause more than one intrinsic parameter becomes indeterminate, and in fact our study confirmed that two parameters (f and c_y) become indeterminate for CPA-1D-GP flight design.

In three real CPA-1D-GP-flight design image sets acquired at three different GSDs, significant variations were observed in the estimated intrinsic parameters - f and c_y - across 30 distinct SfM analysis settings and across 50 repeat trials of a single setting. These results demonstrate that the theoretical indeterminacy of intrinsic parameters observed in numerical experiments, manifests in real-world scenarios as pronounced instability.

This instability likely contributes to the poor performance of image-based SfM observed in previous studies using CPA-1D-GP-flight design's images [19,32], which has often been attributed solely to the dome effect. The present findings indicate that inaccurate estimation of f is also a major contributing factor, leading to large mean vertical errors. Images acquired under CPA-1D-GP flight design, as confirmed in this analysis, significantly compromise the accuracy and precision of image-based SfM and can even lead to incorrect model reconstruction in MVS. Therefore, practical surveys should avoid employing CPA-1D-GP flight design or applying appropriate countermeasure such as augmenting camera coordinates measured by RTK-GNSS or adding many GCPs to ensure stable SfM results when using CPA-1D-GP flight design.

4.4.2. Remedy for indeterminacy of intrinsic parameters in images-based SfM

Numerical experiments demonstrate that adjustments to the shooting positions of CPA-1D-GP flight design, such as a CPA-1D-RP flight design, do not resolve the indeterminacy of intrinsic parameters (f and c_y). However, introducing intermediate strips between primary constant-pitch lines,

as in the CPA-2D-GP flight design, effectively eliminated this indeterminacy in numerical experiments and substantially reduced f and c_y instability in the real-data analysis. This result aligns with the known fact in aerial triangulation that introducing “cross strips” to a block can improve the accuracy of block adjustment [57,58].

This finding suggests that practitioners can largely mitigate concerns regarding the significant instability of intrinsic parameters estimated by image-based SfM by incorporating intermediate strips into CPA-1D-GP flight design. Some built-in flight missions in flight planning software packages automatically include intermediate strips. Such strips can be achieved using timed-interval or distance-interval shot modes, as seen in the 3D photogrammetry function of the DJI P4RTK drone or the “area route” option of the DJI Mavic 3E drone, for example.

In contrast, there are other flight missions that do not include intermediate strips, such as “waypoint” flight, where the camera shutter is triggered at specific pre-defined points. Additionally, some flight planning software, such as Pix4D Capture [19,23,48,59] or Pix4D Capture Pro, does not generate intermediate short strips by default. These choices preserve the CPA-1D-GP critical configuration and risk intrinsic parameters drift. Overall, embedding short cross-strips within CPA-1D-GP flight design prevents indeterminacy of intrinsic parameters, delivering more stable and accurate SfM reconstructions without reliance on camera coordinates measured by RTK-GNSS or extensive GCP networks.

4.4.3. Implications for common flight configurations

The commonly used nadir-viewing flight represents a special case of critical configuration, where the pitch angle is zero. Based on the results presented in this study, such a configuration is also unable to reliably determine the intrinsic parameters, f and c_y .

Although not explicitly analyzed in this study, the results of the CPA-2D-GP flight design imply that, images captured by a “double grid” flight - commonly generated by flight planning software and built-in drone missions - are expected to support the determination of f and c_y . In this “double grid” flight, the images captured in the reverse direction function as intermediate strips, thereby mitigating the indeterminacy of f and c_y .

4.5. Conclusion

This study investigated how certain camera intrinsic parameters in image-based SfM become indeterminate using aerial photos from CPA-1D-GP flight design. Numerical experiments (Section 4.3.1) confirmed that the CPA-1D-GP flight design is a critical configuration that causes the indeterminacy of intrinsic parameters, particularly focal length (f) and principal point coordinate (c_y), under idealized conditions in CG simulation. Further analysis with real data (Section 4.3.2), involving three image-sets over 30 different SfM settings, demonstrated that estimates of f and c_y

are highly unstable when using CPA-1D-GP flight design.

As a countermeasure, the integration of intermediate strips into the CPA-1D-GP flight design - forming a CPA-2D-GP flight design - was shown to eliminate the indeterminacy of intrinsic parameters (f and c_y) in numerical experiments and markedly improve their stability in real-data analyses.

These findings reveal the potential to improve the accuracy of self-calibration using only aerial images in SfM, without the need for GCPs or RTK-GNSS data. This advancement not only simplifies the data acquisition process but also makes it more accessible and cost-effective for practitioners. By stabilizing SfM calibration, all the subsequent stages - such as MVS, dense point cloud generation - can be effectively enhanced, leading to more accurate 3D reconstruction.

This study addressed two fundamental intrinsic parameters, focal length (f) and vertical principal point coordinate (c_y). Future investigations should extend to other intrinsic parameters and explore other critical combinations of camera motion and terrain geometry, as discussed in Chapter 6.

Chapter 5. Impact of in-camera distortion correction on systematic deformation in UAV-based photogrammetry using Structure from Motion

5.1. Introduction

The accuracy of 3D models derived from aerial photogrammetry using UAVs and SfM can be compromised by systematic deformation, commonly referred to as the doming or bowling effect (Fig 5-1). These deformations may result from various factors, with a primary cause being errors in the estimated camera parameters [36].

Lightweight UAV platforms such as those manufactured by DJI, Wingtra, and Trimble commonly employ consumer-grade cameras, which are known for their unstable intrinsic parameters [60]. Consequently, SfM typically relies on self-calibration - estimating intrinsic parameters directly from the image set - rather than using pre-calibrated values obtained under controlled conditions. The Brown distortion model is commonly used in SfM for modeling radial and tangential distortions, under the assumption that no prior image correction has been applied.

However, modern drone-mounted cameras often apply manufacturer-specific geometric adjustments – referred to as in-camera distortion correction - automatically when images are exported and saved in JPEG-format, which are then used in SfM processing. Applying the Brown model to such pre-corrected images may lead to inaccurate estimation of camera parameters, potentially introducing systematic errors into the final model [35]. Notably, James et al. (2014) [36] demonstrated that the magnitude of doming errors in SfM-derived models exhibits a linear relationship with radial distortion, further underscoring the sensitivity of model accuracy to distortion-related preprocessing.

This study aims to evaluate the impact of in-camera distortion correction - executed as image pre-processing prior to SfM - on the systematic deformation in DEMs generated from UAV images. Experiments were conducted using three image sets acquired by a CPA-2D-GP flight design with a 20° pitch angle.

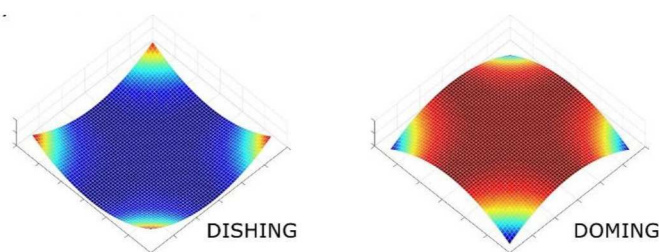


Figure 5-1. Systematic deformation in the form of doming or bowling [15]

5.2. Methods

5.2.1. Data acquisition

This study utilised three image-sets captured by DJI Phantom 4 RTK for a $100 \times 100 \text{ m}^2$ construction-designated area located in Tsukubamirai City, Ibaraki Prefecture, Japan. The details of data acquisition were described in Section 3.2.1 and the specific characteristics of the image-sets used in this study are summarized in Table 5-1.

A Constant-Pitch-Angle, Two-Directional, and Gridded-Position flight design (CPA-2D-GP) was used for data acquisition. The three image-sets were captured with a constant 20° camera pitch angle at three different altitudes - 73 m, 55 m, and 36 m - corresponding to Ground Sampling Distances (GSDs) of 20 mm, 15 mm, and 10 mm, respectively. Each flight maintained an image overlap of 80% in the forward direction and 60% in the side direction.

A total of nine ground markers were distributed throughout the target area using Aerobo markers, each embedded with GNSS receivers capable of providing sub-centimeter positioning accuracy.

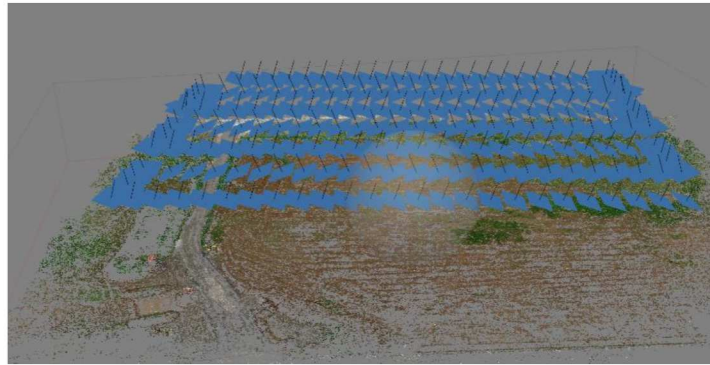


Figure 5-2. Constant-Pitch-Angle, Two-Directional, and Gridded-Position flight design (CPA-2D-GP) at 20° pitch angle (from Metashape).

Table 5-1. Details of raw image sets acquired without in-camera distortion correction. Images were exported in their original (uncorrected) format.

Image-sets	Flight height (m)	Ground sampling distant (mm)	The number of images
1	73	20 (GSD20)	73
2	55	15 (GSD15)	107
3	36	10 (GSD10)	187

5.2.2. Simulation of in-camera distortion correction

To simulate the effect of in-camera image pre-processing, three distortion correction scenarios were defined:

- Scenario 1: Distortion correction using manufacturer-provided camera parameters.
- Scenario 2: Distortion correction using intrinsic parameters estimated from a reference SfM scenario, in which both RTK-GNSS camera coordinates and all ground markers were

incorporated into bundle adjustment.

- Scenario 3: No distortion correction was applied; raw images were used without any geometric adjustments.

This procedure resulted in nine image-sets with three types of distortion correction. These image-sets were then used in SfM processing.

5.2.3. SfM processing and systematic deformation evaluation

SfM processing was performed using Agisoft Metashape (version 1.5.5) following a standard photogrammetric workflow (illustrated in Fig 5-3). Each of the nine image sets (Table 5-1) - consisting of three GSD levels and three distortion correction cases - was processed under two SfM workflows:

- Workflow 1: BA performed using RTK-GNSS camera positions.
- Workflow 2: BA based solely on image data, without any auxiliary positioning information.

In both workflows, sparse point clouds were generated and then georeferenced using the full set of RTK-GNSS camera positions. Subsequently, Digital Elevation Models (DEMs) were produced for all nine image sets under both workflows, resulting in a total of 18 DEMs.

To evaluate systematic deformation - in the form of doming or bowling - each DEM was compared against a corresponding reference DEM. This comparison was performed by generating a differential DEM, defined by Equation (5-1), using QGIS open-source software:

$$\text{DEM}_{\text{difference}} = \text{DEM}_{\text{test}} - \text{DEM}_{\text{reference}} \quad (5-1)$$

Where DEM_{test} : DEM generated from each of nine image-sets.

$\text{DEM}_{\text{reference}}$: DEM generated when all the ground markers and camera coordinates measured by RTK-GNSS were used in BA. These reference DEMs are regarded as the most reliable representations for each raw image set.

The occurrence of systematic deformation (doming/bowling) is identified through visualizing the differential DEM, as shown in Fig 5-4. If the center of the differential DEM exhibits a higher elevation than the surrounding area, the original DEM is considered to display doming deformation. Conversely, if the center is lower than its surroundings, it indicates bowling deformation. A relatively flat differential DEM suggests the absence of systematic deformation.

To quantify the magnitude of deformation, the elevation range between the 95th and 5th percentile pixel values within the differential DEM was calculated:

$$\text{Deformation magnitude} = 95^{\text{th}} \text{ percentile} - 5^{\text{th}} \text{ percentile} \quad (5-2)$$

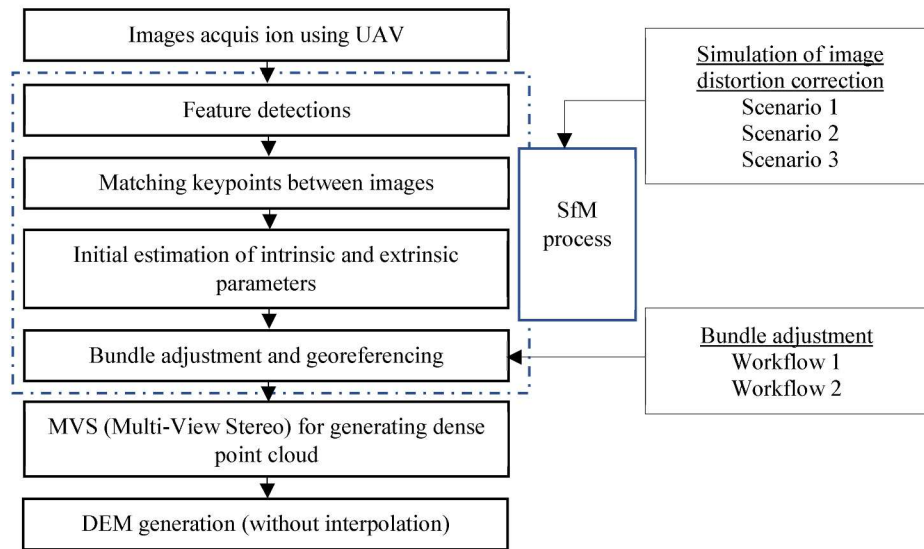


Figure 5-3. SfM workflow and research procedure

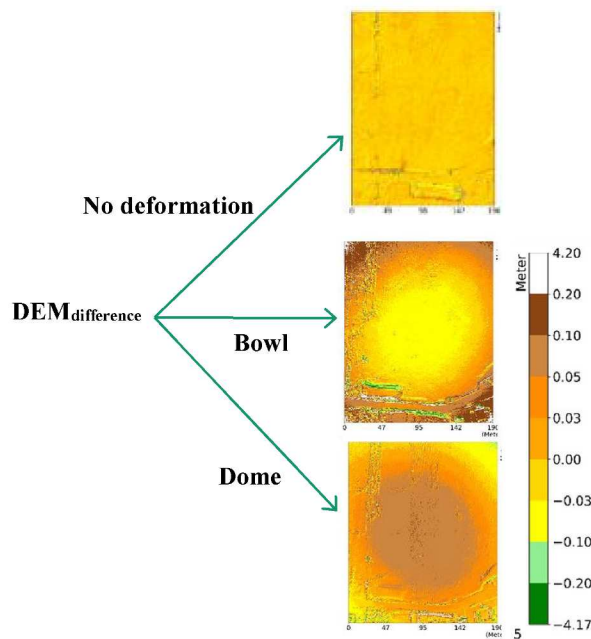


Figure 5-4. Identifying systematic deformation through visualization of the differential DEM

The 5th and 95th percentiles were selected to represent the vertical error at the lower and upper ends of the error distribution, corresponding to the "bottom" and "peak" of deformation, respectively. These percentiles were chosen - rather than the minimum and maximum values - to reduce the influence of outliers.

5.3. Results and discussion

5.3.1. Differences between the reference DEMs and DEMs with in-camera distortion correction

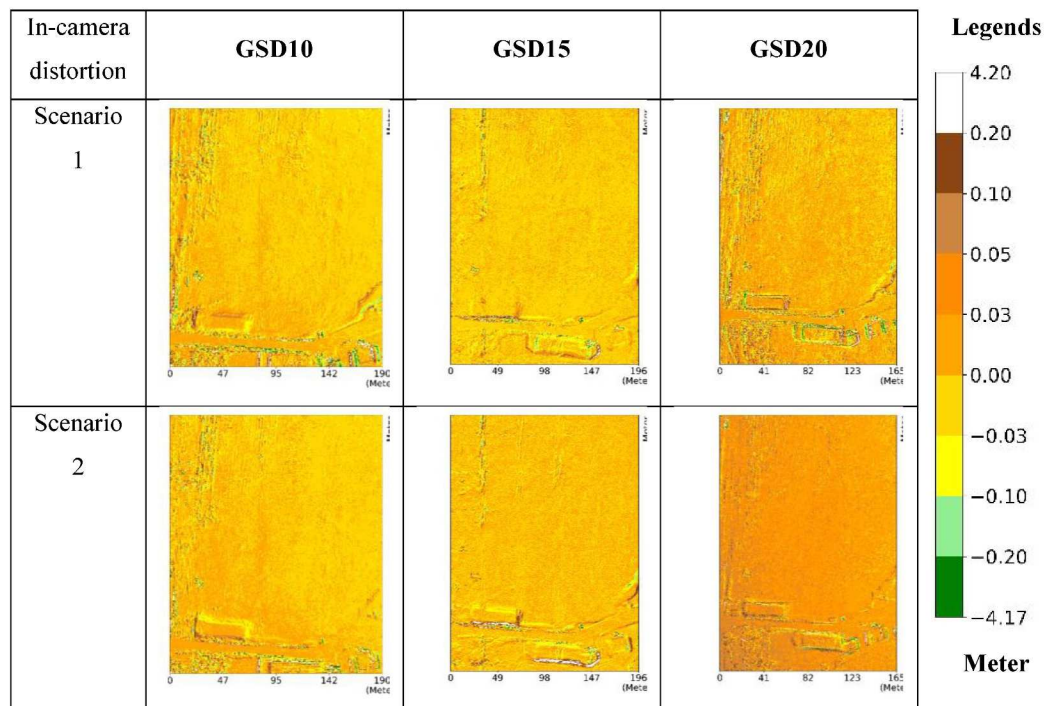
Table 5-2 presents the differential DEM results for three image sets captured at three GSDs, each processed under the three defined distortion correction scenarios. The findings indicate that when bundle adjustment incorporates accurate camera positions measured by RTK-GNSS (workflow 1), the resulting DEMs_{test} exhibit consistent elevation differences across the entire study area when compared to the reference DEM.

This consistency confirms the absence of systematic deformation, regardless of whether in-camera distortion correction was applied to the images prior to the SfM process.

In contrast, when the bundle adjustment process relies solely on image data (image-based SfM) - without integrating auxiliary data such as Ground Control Points (GCPs) or camera coordinates obtained from RTK-GNSS - the resulting DEMs exhibit systematic deformation, as illustrated in Table 5-3.

These findings indicate that the observed systematic deformation in SfM-derived DEMs originates from self-calibration, specially the optimization of camera parameters in the absence of precise external constraints.

Table 5-2. Differential DEMs calculated from Workflow 1: Bundle adjustment using RTK-GNSS camera positions.



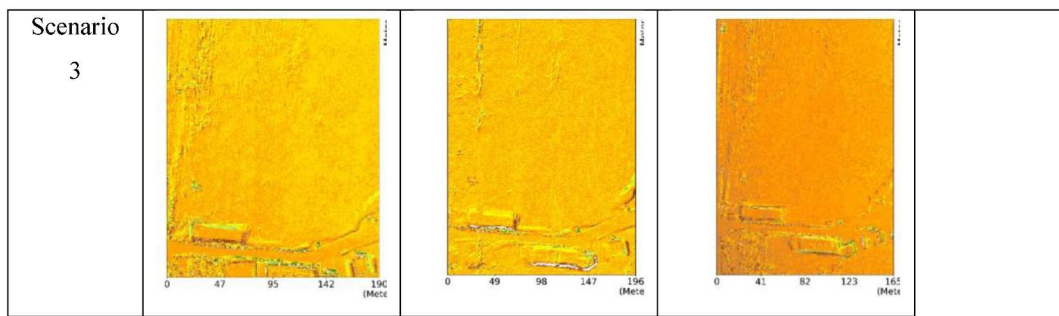
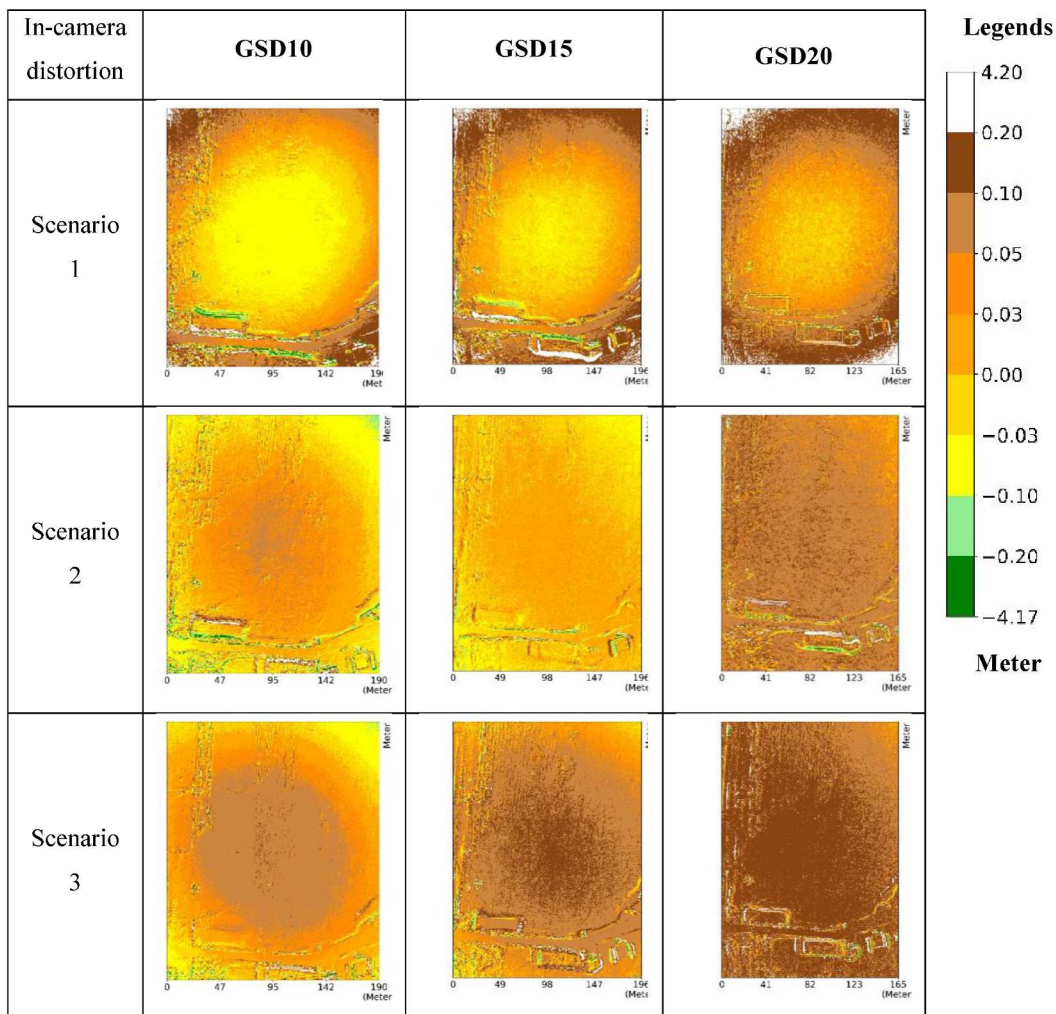


Table 5-3. Differential DEMs calculated from Workflow 2: Bundle adjustment using images only.



5.3.2. Evaluation of the magnitude of deformation

For image-sets processed under Workflow 2, where bundle adjustment was performed without auxiliary data and deformation was observed, the magnitude of DEM deformation was quantified for each of the distortion correction scenarios.

Initially, the histogram and spatial distribution of 95th percentile pixel values and 5th percentile

pixel values in DEM_{difference} were examined to assess whether these percentiles reliably represented the "peak" and "bottom" of the deformation, respectively.

As shown in Table 5-4, the 5th and 95th percentiles did not consistently reflect the true elevation extremes, partially owing to the non-ground objects in the target area.

Table 5-4. Spatial distribution of 95th percentile pixel values (Red) and 5th percentile pixel values (blue) in DEM_{difference} for Workflow 2.

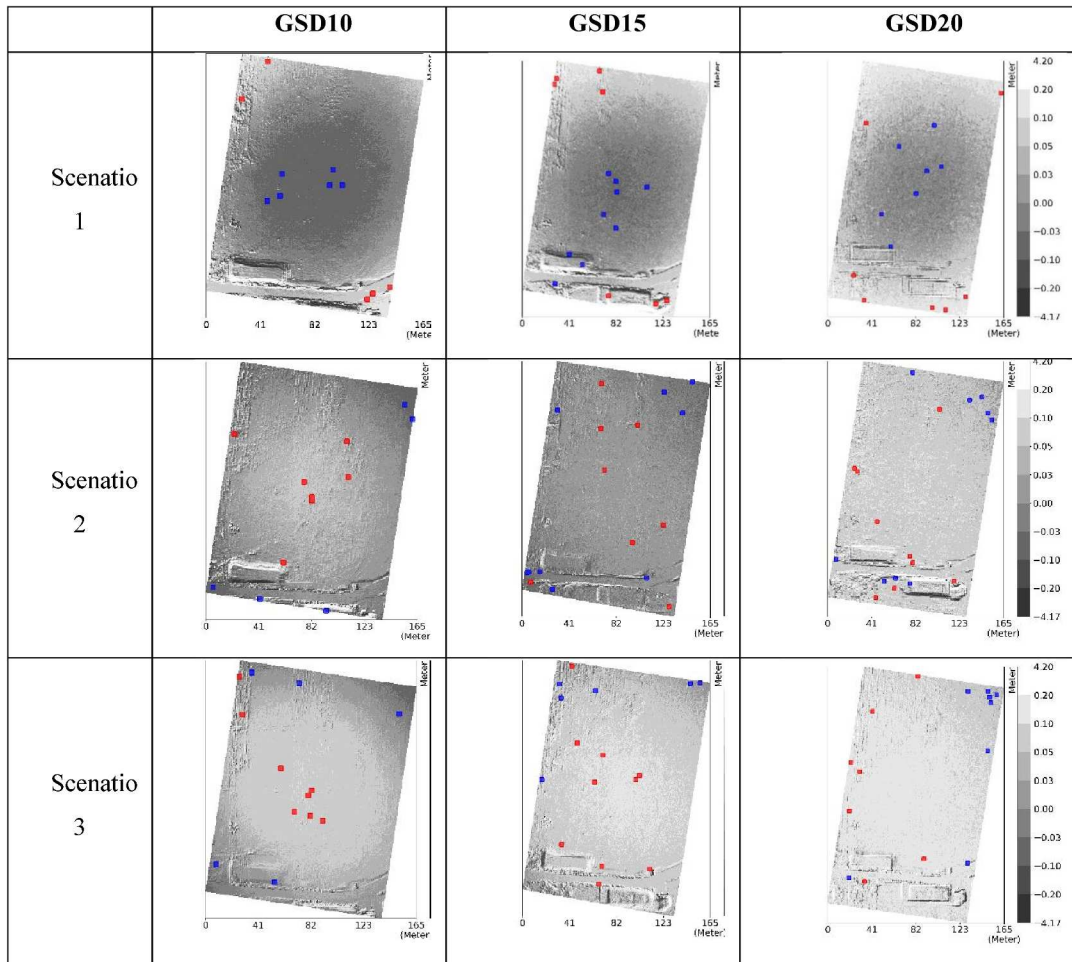
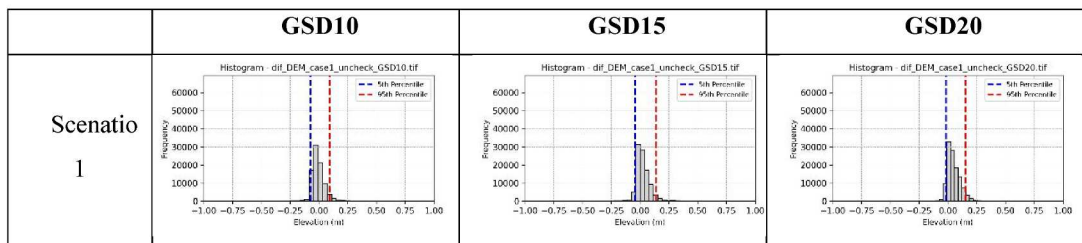
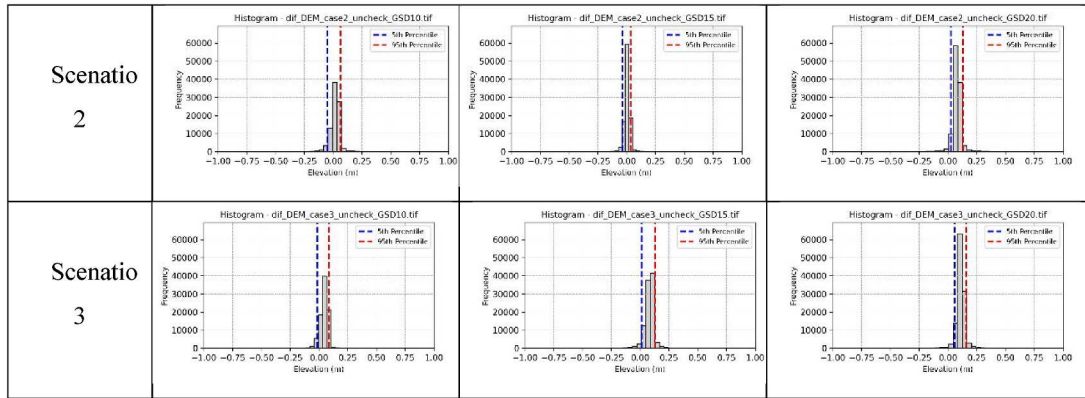


Table 5-5. Histograms of pixel values of DEM_{difference} with 95th percentile (Red) and 5th percentile (blue) for Workflow 2.





To address this issue, a slope filter was applied prior to percentile calculation. This filter excludes pixels whose maximum local slope (defined as the maximum elevation difference between a center pixel and its 8 surrounding pixels, divided by the GSD) exceeded a certain threshold (1):

$$\text{Maximum local slope} = \max \left(\frac{|\text{neighbor pixel} - \text{center pixel}|}{\text{GSD}} \right)$$

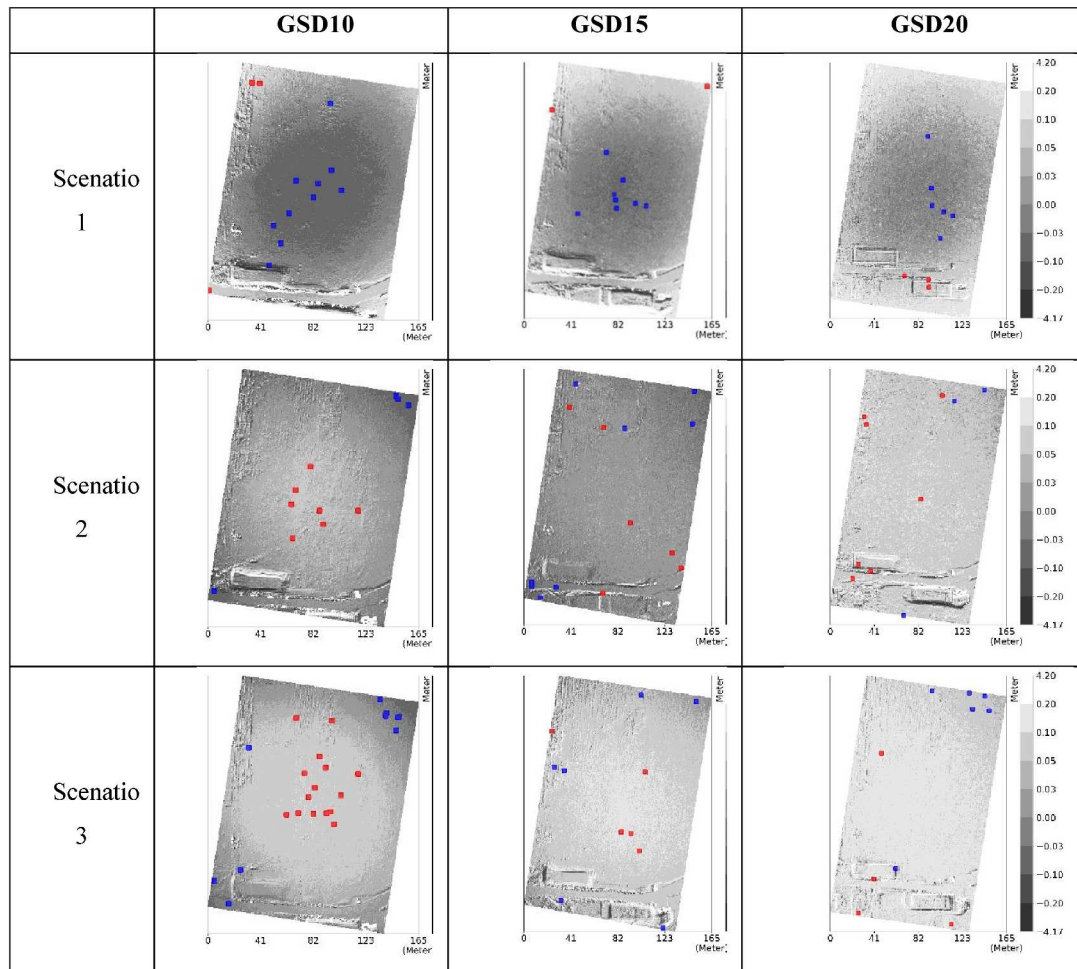
Where:

- Center pixel: pixel used to calculate the maximum local slope (m)
- Neighbor pixel: 8 pixels surrounding the center pixel (m)
- GSD: ground sample distance (m)

After applying this filter, the results (Table 5-6) showed that, although the filtered percentiles visually aligned with the elevation differences in some cases - such as Scenario 1 (GSD 10, 15, 20), Scenario 2 (GSD 10), and Scenario 3 (GSD 10) - they still did not consistently or accurately capture the elevation differences between the center and surrounding areas.

Further research is needed to develop a more robust and spatially representative metric for evaluating magnitude of systematic deformation in DEMs.

Table 5-6. Spatial distribution of 95th percentile pixel values (Red) and 5th percentile pixel values (blue) in DEM_{difference} for Workflow 2, after applying maximum local slope filtering.



5.4. Conclusion

In this study, three image sets captured using the Constant-Pitch-Angle, Two-Directional, and Gridded-Position flight design (CPA-2D-GP) - with a constant 20° pitch angle at three different altitudes - were used to investigate the impact of in-camera distortion correction on systematic deformation in DEMs generated by SfM. The results demonstrate that systematic deformation occurs regardless of whether in-camera distortion correction was applied prior to image-based SfM process.

Additionally, the findings emphasize the critical importance of incorporating auxiliary data - high-precision camera coordinates obtained via RTK-GNSS - into the SfM workflow to effectively suppress such deformations.

Chapter 6. Conclusion and future research

6.1. Conclusion

This dissertation investigated critical challenges associated with the indeterminacy and inaccuracy of intrinsic camera parameters in UAV-based photogrammetry using SfM. The focus was on identifying the causes of these issues and proposing practical strategies to improve the reliability of image-based SfM, particularly in scenarios where auxiliary information such as camera coordinates measured by RTK-GNSS or GCPs is limited or unavailable.

In **Chapter 3**, the robustness of SfM accuracy and precision against non-optimal SfM analysis settings was assessed using a widely adopted UAV flight design: the Constant-Pitch-Angle, Two-Directional, and Gridded-Position (CPA-2D-GP). Through an extensive analysis of 750 settings across 15 image-sets, the results demonstrated that 20° and 30° pitch angles consistently yielded high accuracy and precision in SfM. These findings confirmed the generality of the robustness of CPA-2D-GP flight design, as suggested in previous research.

In **Chapter 4**, the indeterminacy of intrinsic parameters, particularly focal length (f) and vertical principal point coordinate (cy) was demonstrated through numerical experiments using images captured by Constant-Pitch-Angle, One-Directional, and Gridded-Position (CPA-1D-GP) flight designs. The experiments showed that this flight configuration represents a critical configuration in which f and cy become indeterminable in image-based SfM. These findings were validated with real UAV data, showing significant variability in intrinsic parameter estimates (f and cy) across multiple SfM settings and repeated trials of a single setting. The incorporation of intermediate strips, transitioning from CPA-1D-GP to CPA-2D-GP flight design, effectively mitigated this indeterminacy. This strategy improves the stability of intrinsic parameter estimation (f and cy) without the need for auxiliary data in bundle adjustment.

In **Chapter 5**, the impact of in-camera distortion correction on systematic deformation in digital elevation models (DEMs) was examined using three CPA-2D-GP image-sets. The study showed that systematic deformations (doming/bowling) occur regardless of whether distortion correction is applied prior to SfM process, if bundle adjustment was performed using images only. However, when RTK-GNSS camera coordinates were integrated into bundle adjustment, the deformations were effectively suppressed.

In summary, the research contributes to a deeper understanding of how flight design, SfM analysis settings, and image preprocessing practices affect the accuracy, stability, and reliability of UAV-based photogrammetry using SfM. It also proposes practical and experimentally validated strategies to mitigate these issues.

6.2. Future research

It is crucial to understand that the best pitch angles for UAV-based data acquisition, which can be robust against non-optimal SfM analysis settings, may vary depending on the characteristics of the target area. In this study, a flat terrain with minimal vegetation was selected as a baseline to establish foundational insights. However, future investigations should extend these findings to more complex environments, such as steep slopes, undulating topographies, or densely vegetated areas, to assess whether similar robustness patterns hold under varied terrain conditions.

Additionally, this study examined the robustness of SfM accuracy and precision for CPA-2D-GP flight design without the use of ground control points (GCPs), by incorporating RTK-GNSS camera positions for bundle adjustment and georeferencing. Further investigation is necessary to evaluate the robustness of SfM accuracy and precision in scenarios where only GCPs are available, particularly when using drones that lack onboard RTK-GNSS receiver.

Given that the accuracy and precision of SfM are highly sensitive to analysis settings, it is advisable to evaluate SfM performance using a range of analysis settings, rather than relying solely on a single standard setting. This approach helps ensure optimal camera parameter estimation for a given image set.

This dissertation also initiated the investigation of intrinsic parameter indeterminacy with a focus on two fundamental intrinsic parameters: focal length (f) and vertical principal point coordinate (c_y). Future studies should extend this analysis to include other intrinsic parameters, such as the horizontal principal point (c_x) and nonlinear distortion coefficients, whose instability may also compromise SfM outcomes.

Moreover, beyond the CPA-1D-GP flight design, other combinations of camera motion and scene geometry may also constitute critical configurations that result in indeterminate intrinsic parameters. Identifying and characterizing these configurations, both theoretically and empirically, is essential for improving the reliability for SfM with self-calibration.

Such efforts will advance UAV-based photogrammetry using SfM toward greater reliability, cost-effectiveness, and adaptability across diverse terrain conditions, making it suitable for a wide range of applications.

References

1. Tomašík, J.; Mokoš, M.; Saloš, S.; Chudý, F.; Tunák, D. Accuracy of Photogrammetric UAV-Based Point Clouds under Conditions of Partially-Open Forest Canopy. *Forests* 2017, 8, doi:10.3390/f8050151.
2. Kim, D.W.; Yun, H.S.; Jeong, S.J.; Kwon, Y.S.; Kim, S.G.; Lee, W.S.; Kim, H.J. Modeling and Testing of Growth Status for Chinese Cabbage and White Radish with UAV-Based RGB Imagery. *Remote Sens (Basel)* 2018, 10, doi:10.3390/rs10040563.
3. Coveney, S.; Roberts, K. Lightweight UAV Digital Elevation Models and Orthoimagery for Environmental Applications: Data Accuracy Evaluation and Potential for River Flood Risk Modelling. *Int J Remote Sens* 2017, 38, 3159–3180, doi:10.1080/01431161.2017.1292074.
4. Fernando Carvajal-Ramírez, F.A.-V.P.J.M.-C. Effects of Image Orientation and Ground Control Points Distribution on Unmanned Aerial Vehicle Photogrammetry Projects on a Road Cut Slope. *J Appl Remote Sens* 2016, 10.
5. Godone, D.; Allasia, P.; Borrelli, L.; Gullà, G. UAV and Structure from Motion Approach to Monitor the Maierato Landslide Evolution. *Remote Sens (Basel)* 2020, 12, doi:10.3390/rs12061039.
6. Kršák, B.; Blišťan, P.; Pauliková, A.; Puškárová, P.; Kovanič, L.; Palková, J.; Zelizňaková, V. Use of Low-Cost UAV Photogrammetry to Analyze the Accuracy of a Digital Elevation Model in a Case Study. *Measurement (Lond)* 2016, 91, 276–287, doi:10.1016/j.measurement.2016.05.028.
7. Partama, I.G.Y.; Kanno, A.; Ueda, M.; Akamatsu, Y.; Inui, R.; Sekine, M.; Yamamoto, K.; Imai, T.; Higuchi, T. Removal of Water-Surface Reflection Effects with a Temporal Minimum Filter for UAV-Based Shallow-Water Photogrammetry. *Earth Surf Process Landf* 2018, 43, 2673–2682.
8. Woodget, A.S.; Carbonneau, P.E.; Visser, F.; Maddock, I.P. Quantifying Submerged Fluvial Topography Using Hyperspatial Resolution UAS Imagery and Structure from Motion Photogrammetry. *Earth Surf Process Landf* 2015, 40, 47–64, doi:10.1002/esp.3613.
9. Smith, M.W.; Vericat, D. From Experimental Plots to Experimental Landscapes: Topography, Erosion and Deposition in Sub-Humid Badlands from Structure-from-Motion Photogrammetry. *Earth Surf Process Landf* 2015, 40, 1656–1671, doi:10.1002/esp.3747.
10. Sanz-Ablanedo, E.; Chandler, J.H.; Rodríguez-Pérez, J.R.; Ordóñez, C. Accuracy of Unmanned Aerial Vehicle (UAV) and SfM Photogrammetry Survey as a Function of the Number and Location of Ground Control Points Used. *Remote Sens (Basel)* 2018, 10, doi:10.3390/rs10101606.
11. Zhong, H.; Duan, Y.; Tao, P.; Zhang, Z. Influence of Ground Control Point Reliability and Distribution on UAV Photogrammetric 3D Mapping Accuracy. *Geo-spatial Information Science* 2025, 1–21, doi:10.1080/10095020.2025.2451204.
12. Sanz-Ablanedo, E.; Chandler, J.H.; Rodríguez-Pérez, J.R.; Ordóñez, C. Accuracy of Unmanned Aerial Vehicle (UAV) and SfM Photogrammetry Survey as a Function of the Number and Location of Ground Control Points Used. *Remote Sens (Basel)* 2018, 10, doi:10.3390/rs10101606.
13. Deliry, S.I.; Avdan, U. Accuracy Assessment of UAS Photogrammetry and Structure from Motion in Surveying and Mapping. *International Journal of Engineering and Geosciences* 2024, 9, 165–190, doi:10.26833/ijeg.1366146.

14. Štroner, M.; Urban, R.; Seidl, J.; Reindl, T.; Brouček, J. Photogrammetry Using UAV-Mounted GNSS RTK: Georeferencing Strategies without GCPs. *Remote Sens (Basel)* 2021, 13, doi:10.3390/rs13071336.
15. Carbonneau, P.E.; Dietrich, J.T. Cost-Effective Non-Metric Photogrammetry from Consumer-Grade SUAS: Implications for Direct Georeferencing of Structure from Motion Photogrammetry. *Earth Surf Process Landf* 2017, 42, 473–486, doi:10.1002/esp.4012.
16. James, M.R.; Robson, S.; Smith, M.W. 3-D Uncertainty-Based Topographic Change Detection with Structure-from-Motion Photogrammetry: Precision Maps for Ground Control and Directly Georeferenced Surveys. *Earth Surf Process Landf* 2017, 42, 1769–1788, doi:10.1002/esp.4125.
17. Sanz-Ablanedo, E.; Chandler, J.H.; Ballesteros-Pérez, P.; Rodríguez-Pérez, J.R. Reducing Systematic Dome Errors in Digital Elevation Models through Better UAV Flight Design. *Earth Surf Process Landf* 2020, 45, 2134–2147, doi:10.1002/ESP.4871.
18. Luo, W.; Shao, M.; Che, X.; Hesp, P.A.; Bryant, R.G.; Yan, C.; Xing, Z. Optimization of UAVs-SfM Data Collection in Aeolian Landform Morphodynamics: A Case Study from the Gonghe Basin, China. *Earth Surf Process Landf* 2020, 45, 3293–3312, doi:10.1002/esp.4965.
19. Sanz-Ablanedo, E.; Chandler, J.H.; Ballesteros-Pérez, P.; Rodríguez-Pérez, J.R. Reducing Systematic Dome Errors in Digital Elevation Models through Better UAV Flight Design. *Earth Surf Process Landf* 2020, 45, 2134–2147, doi:10.1002/esp.4871.
20. Ariyo Kanno; Matsuoka Yuji; Yuki Otsu; Kazuo Sugimoto; Masaya Takada Effect of Constant Pitch Meandering Flight Method and Analysis Settings in SfM without GCPs (Translated from Japanese). *Proceedings of JSPRS Annual Conference 2021 (日本写真測量学会令和3年度秋季学術講演会発表論文集)* 2021, 49–52.
21. Ariyo, K.; Junnosuke, K.; Truc, T.H.; Masaki, H.; Tatsuji, F.; Kyouhei, K. Accuracy Verification Experiment of UAV Photogrammetry Using Optical Axis Optimization Shooting with Airpeak S1 + A7III(Translated from Japanese). *Proceedings of JSPRS Annual Conference 2022 (日本写真測量学会令和4年度秋季学術講演会発表論文集)* 2022, 41–42.
22. Truc, T.H.; Ariyo, K.; Yuji, M.; Masahiko, S.; Tsuyoshi, I.; Koichi, Y.; Takaya, H. Robustness of Structure from Motion Accuracy/Precision against the Non-Optimality in Analysis Settings: Case Study in Constant-Pitch Flight Design. *Int. J. of Automation Technology* 2024, 18.
23. Nesbit, P.R.; Hugenholtz, C.H. Enhancing UAV-SfM 3D Model Accuracy in High-Relief Landscapes by Incorporating Oblique Images. *Remote Sens (Basel)* 2019, 11, doi:10.3390/rs11030239.
24. Ariyo, K.; Matsuoka, Y.; Yuki, O.; Kazuo, S.; Masaya, T. Effect of Constant Pitch Meandering Flight Method and Analysis Settings in SfM without GCPs (Translated from Japanese). *Proceedings of JSPRS Annual Conference 2021 (日本写真測量学会平成29年度秋季学術講演会発表論文集)* 2021, 49–52.
25. C.S. Fraser; S. Al-Ajlouni Zoom-Dependent Camera Calibration in Digital Close-Range Photogrammetry. *Photogramm Eng Remote Sensing* 2006, 72, 1017–1026.
26. Fraser, C.S. *PHOTOGRAMMETRY & REMOTE SENSING Digital Camera Self-Calibration*; 1997;

Vol. 52;.

27. Abeho, D.R.; Shoko, M.; Odera, P.A. Effects of Camera Calibration on the Accuracy of Unmanned Aerial Vehicle Sensor Products. *International Journal of Engineering and Geosciences* 2024, doi:10.26833/ijeg.1422619.
28. Senn, J.A.; Mills, J.; Walsh, C.L.; Addy, S.; Peppas, M. On-site Geometric Calibration of RPAS Mounted Sensors for SfM Photogrammetric Geomorphological Surveys. *Earth Surf Process Landf* 2022, 47, 1615–1634, doi:10.1002/esp.5338.
29. Daakir, M.; Zhou, Y.; Pierrot Deseilligny, M.; Thom, C.; Martin, O.; Rupnik, E. Improvement of Photogrammetric Accuracy by Modeling and Correcting the Thermal Effect on Camera Calibration. *ISPRS Journal of Photogrammetry and Remote Sensing* 2019, 148, 142–155, doi:10.1016/j.isprsjprs.2018.12.012.
30. Elias, M.; Eltner, A.; Liebold, F.; Maas, H.-G. Assessing the Influence of Temperature Changes on the Geometric Stability of Smartphone- and Raspberry Pi Cameras. *Sensors* 2020, 20, 643, doi:10.3390/s20030643.
31. Smith, M.J.; Cope, E. The Effects of Temperature Variation on Single-Lens-Reflex Digital Camera Calibration Parameters. In Proceedings of the International Archives of Photogrammetry, Remote Sensing and Spatial Information Sciences, Vol. XXXVIII, Part 5 Commission V Symposium; Newcastle upon Tyne< UK, 2010; Vol. XXXVIII, p. 554559.
32. Junnosuke Kon; Ariyo Kanno; Masaki Haruna; Tatsuji Fujii; Kyouhei Kurita The Robustness of SfM Settings and Vulnerability to Dome-Shaped Deformation in Four Types of UAV Oblique Photography Methods. (Translated from Japanese). *Proceedings of JSPRS Annual Conference 2023 (日本写真測量学会令和5年度春季学術講演会発表論文集)* 2023, 37–38.
33. Hartley, R.; Zisserman, A. *Multiple View Geometry in Computer Vision*; Second.; Cambridge University Press, 2004; ISBN 9780521540513.
34. Brown, D.C. Close-Range Camera Calibration. *Photogrammetric Engineering* 1971, 37, 855–866.
35. James, M.R.; Antoniazza, G.; Robson, S.; Lane, S.N. Mitigating Systematic Error in Topographic Models for Geomorphic Change Detection: Accuracy, Precision and Considerations beyond off-Nadir Imagery. *Earth Surf Process Landf* 2020, 45, 2251–2271, doi:10.1002/esp.4878.
36. James, M.R.; Robson, S. Mitigating Systematic Error in Topographic Models Derived from UAV and Ground-Based Image Networks. *Earth Surf Process Landf* 2014, 39, 1413–1420, doi:10.1002/esp.3609.
37. Brown, D.C. Close-Range Camera Calibration. *Photogrammetric Engineering* 1971, 37, 855–866.
38. James, M.R.; Robson, S. Straightforward Reconstruction of 3D Surfaces and Topography with a Camera: Accuracy and Geoscience Application. *J Geophys Res Earth Surf* 2012, 117, doi:10.1029/2011JF002289.
39. Snavely, N.; Seitz, S.M.; Szeliski, R. Modeling the World from Internet Photo Collections. *Int J Comput Vis* 2008, 80, 189–210, doi:10.1007/s11263-007-0107-3.
40. Lowe, D.G. Distinctive Image Features from Scale-Invariant Keypoints. *Int J Comput Vis* 2004, 60, 91–110, doi:10.1023/B:VISI.0000029664.99615.94.
41. Nesbit, P.R.; Hugenholtz, C.H. Enhancing UAV-SfM 3D Model Accuracy in High-Relief Landscapes

- by Incorporating Oblique Images. *Remote Sens (Basel)* 2019, *11*, doi:10.3390/rs11030239.
42. Eltner, A.; Baumgart, P.; Maas, H.G.; Faust, D. Multi-Temporal UAV Data for Automatic Measurement of Rill and Interrill Erosion on Loess Soil. *Earth Surf Process Landf* 2015, *40*, 741–755, doi:10.1002/esp.3673.
 43. Deliry, S.I.; Avdan, U. Accuracy of Unmanned Aerial Systems Photogrammetry and Structure from Motion in Surveying and Mapping: A Review. *Journal of the Indian Society of Remote Sensing* 2021, *49*, 1997–2017.
 44. Aerosense Inc. AeroBo Marker Available online: https://aerosense.co.jp/en/products/equipment_systems/ (accessed on 19 November 2024).
 45. Cramer, M.; Przybilla, H.J.; Zuerhorst, A. UAV Cameras: Overview and Geometric Calibration Benchmark. In Proceedings of the International Archives of the Photogrammetry, Remote Sensing and Spatial Information Sciences - ISPRS Archives; International Society for Photogrammetry and Remote Sensing, August 23 2017; Vol. 42, pp. 85–92.
 46. James, M.R.; Chandler, J.H.; Eltner, A.; Fraser, C.; Miller, P.E.; Mills, J.P.; Noble, T.; Robson, S.; Lane, S.N. Guidelines on the Use of Structure-from-Motion Photogrammetry in Geomorphic Research. *Earth Surf Process Landf* 2019, *44*, 2081–2084, doi:10.1002/esp.4637.
 47. Bemis, S.P.; Micklethwaite, S.; Turner, D.; James, M.R.; Akciz, S.; Thiele, S.; Bangash, H.A. Ground-Based and UAV-Based Photogrammetry: A Multi-Scale, High-Resolution Mapping Tool for Structural Geology and Paleoseismology. *J Struct Geol* 2014, *69*, 163–178.
 48. Ahmed, S.; El-Shazly, A.; Abed, F.; Ahmed, W. The Influence of Flight Direction and Camera Orientation on the Quality Products of UAV-Based SfM-Photogrammetry. *Applied Sciences (Switzerland)* 2022, *12*, doi:10.3390/app122010492.
 49. Moreels, P.; Perona, P. Evaluation of Features Detectors and Descriptors Based on 3D Objects. *Int J Comput Vis* 2007, *73*, 263–284, doi:10.1007/s11263-006-9967-1.
 50. Liu, Y.; Han, K.; Rasdorf, W. Assessment and Prediction of Impact of Flight Configuration Factors on UAS-Based Photogrammetric Survey Accuracy. *Remote Sens (Basel)* 2022, *14*, doi:10.3390/rs14164119.
 51. Blender Foundation Blender 2.79 Release Notes.
 52. James, M.R.; Robson, S. Mitigating Systematic Error in Topographic Models Derived from UAV and Ground-Based Image Networks. *Earth Surf Process Landf* 2014, *39*, 1413–1420, doi:10.1002/esp.3609.
 53. Dai, W.; Zheng, G.; Antoniazza, G.; Zhao, F.; Chen, K.; Lu, W.; Lane, S.N. Improving UAV-SfM Photogrammetry for Modelling High-relief Terrain: Image Collection Strategies and Ground Control Quantity. *Earth Surf Process Landf* 2023, *48*, 2884–2899, doi:10.1002/esp.5665.
 54. DJI Enterprise Phantom 4 RTK Available online: <https://www.dji.com/jp/support/product/phantom-4-rtk> (accessed on 19 November 2024).
 55. James, M.R.; Chandler, J.H.; Eltner, A.; Fraser, C.; Miller, P.E.; Mills, J.P.; Noble, T.; Robson, S.; Lane, S.N. Guidelines on the Use of Structure-from-Motion Photogrammetry in Geomorphic Research. *Earth Surf Process Landf* 2019, *44*, 2081–2084, doi:10.1002/esp.4637.
 56. Kahl, F.; Triggs, B.; Åström, K. Critical Motions for Auto-Calibration When Some Intrinsic

- Parameters Can Vary. *J Math Imaging Vis* 2000, 13, 131–146, doi:10.1023/A:1026524030731.
57. Fackermann; HSchade Application of GPS for Aerial Triangulation. *Photogramm Eng Remote Sensing* 1993, 59, 1625–1632.
 58. Forstner, W. The Reliability of Block Triangulation. *Photogramm Eng Remote Sensing* 1985, 51, 1137–1149.
 59. Iheaturu, C.; Okolie, C.; Ayodele, E.; Egogo-Stanley, A.; Musa, S.; Ifejika Speranza, C. A Simplified Structure-from-Motion Photogrammetry Approach for Urban Development Analysis. *Remote Sens Appl* 2022, 28, 100850, doi:10.1016/j.rsase.2022.100850.
 60. Cramer, M.; Przybilla, H.J.; Zurhorst, A. UAV Cameras: Overview and Geometric Calibration Benchmark. In Proceedings of the International Archives of the Photogrammetry, Remote Sensing and Spatial Information Sciences - ISPRS Archives; International Society for Photogrammetry and Remote Sensing, August 23 2017; Vol. 42, pp. 85–92.